

## THE STAR FORMATION IN RADIO SURVEY: GBT 33 GHz OBSERVATIONS OF NEARBY GALAXY NUCLEI AND EXTRANUCLEAR STAR-FORMING REGIONS

E.J. MURPHY<sup>1</sup>, J. BREMSETH<sup>2</sup>, B.S. MASON<sup>3</sup>, J.J. CONDON<sup>3</sup>, E. SCHINNERER<sup>4</sup>, G. ANIANO<sup>5</sup>, L. ARMUS<sup>5</sup>, G. HELOU<sup>6</sup>,  
J.L. TURNER<sup>7</sup>, T.H. JARRETT<sup>8</sup>

*Submitted to ApJ July 16, 2012; Accepted October 10, 2012*

### ABSTRACT

We present 33 GHz photometry of 103 galaxy nuclei and extranuclear star-forming complexes taken with the Green Bank Telescope (GBT) as part of the Star Formation in Radio Survey (SFRS). Among the sources without evidence for an AGN, and also having lower frequency radio data, we find a median thermal fraction at 33 GHz of  $\approx 76\%$  with a dispersion of  $\approx 24\%$ . For all sources resolved on scales  $\lesssim 0.5$  kpc, the thermal fraction is even larger, being  $\gtrsim 90\%$ . This suggests that the rest-frame 33 GHz emission provides a sensitive measure of the ionizing photon rate from young star-forming regions, thus making it a robust star formation rate indicator. Taking the 33 GHz star formation rates as a reference, we investigate other empirical calibrations relying on different combinations of warm 24  $\mu$ m dust, total infrared (IR; 8 – 1000  $\mu$ m), H $\alpha$  line, and far-UV continuum emission. The recipes derived here generally agree with others found in the literature, albeit with a large dispersion that most likely stems from a combination of effects. Comparing the 33 GHz to total IR flux ratios as a function of the radio spectral index, measured between 1.7 and 33 GHz, we find that the ratio increases as the radio spectral index flattens which does not appear to be a distance effect. Consequently, the ratio of non-thermal to total IR emission appears relatively constant, suggesting only moderate variations in the cosmic-ray electron injection spectrum and ratio of synchrotron to total cooling processes among star-forming complexes. Assuming that this trend solely arises from an increase in the thermal fraction sets a maximum on the scatter of the non-thermal spectral indices among the star-forming regions of  $\sigma_{\alpha_{\text{NT}}} \lesssim 0.13$ .

*Subject headings:* galaxies: nuclei – HII regions – radio continuum: general – stars: formation

### 1. INTRODUCTION

Radio emission from galaxies is powered by a combination of distinct physical processes. And although it is energetically weak with respect to a galaxy’s bolometric luminosity, it provides critical information on the massive star formation activity, as well as access to the relativistic [magnetic field + cosmic rays (CRs)] component in the interstellar medium (ISM) of galaxies.

Stars more massive than  $\sim 8 M_{\odot}$  end their lives as core-collapse supernovae, whose remnants are thought to be the primary accelerators of CR electrons (e.g., Koyama et al. 1995) giving rise to the diffuse synchrotron emission observed from star-forming galaxies (Condon 1992). These same massive stars are also responsible for the creation of HII regions that produce radio free-free

emission, whose strength is directly proportional to the production rate of ionizing (Lyman continuum) photons.

Microwave frequencies, nominally spanning  $\sim 1$  – 100 GHz and observable from the ground, are particularly useful in probing such processes. The non-thermal emission component typically has a steep spectrum ( $S_{\nu} \propto \nu^{-\alpha}$ , where  $\alpha \sim 0.8$ ), while the thermal (free-free) component is relatively flat ( $\alpha \sim 0.1$ ). Accordingly, for globally integrated measurements of star-forming galaxies, lower frequencies (e.g., 1.4 GHz) are generally dominated by non-thermal emission, while the observed thermal fraction of the emission increases with frequency, eventually being dominated by free-free emission once beyond  $\sim 30$  GHz (Condon & Yin 1990). For typical HII regions, the thermal fraction at 33 GHz can be considerably higher, being  $\sim 80\%$  (Murphy et al. 2011). Thus, observations at such frequencies, which are largely unbiased by dust, provide an excellent diagnostic for the current star formation rate (SFR) of galaxies.

It is worth noting that the presence of an “anomalous” emission component in excess of free-free emission between  $\sim 10$  and 90 GHz, generally attributed to electric dipole rotational emission from ultrasmall ( $a \lesssim 10^{-6}$  cm) grains (e.g., Erickson 1957; Draine & Lazarian 1998a,b; Planck Collaboration et al. 2011) or magnetic dipole emission from thermal fluctuations in the magnetization of interstellar dust grains (Draine & Lazarian 1999), may complicate this picture. For a single outerdisk star-forming region in NGC 6946, Murphy et al. (2010) reported an excess of 33 GHz emission relative to what is expected given existing lower frequency radio

<sup>1</sup> Observatories of the Carnegie Institution for Science, 813 Santa Barbara Street, Pasadena, CA 91101, USA; emurphy@obs.carnegiescience.edu

<sup>2</sup> Department of Physics and Astronomy, Pomona College, Claremont, CA 91711, USA

<sup>3</sup> National Radio Astronomy Observatory, 520 Edgemont Road, Charlottesville, VA 22903, USA

<sup>4</sup> Max Planck Institut für Astronomie, Königstuhl 17, Heidelberg D-69117, Germany

<sup>5</sup> Department of Astrophysical Sciences, Princeton University, Princeton, NJ 08544, USA

<sup>5</sup> *Spitzer Science Center*, California Institute of Technology, MC 314-6, Pasadena CA, USA

<sup>6</sup> California Institute of Technology, MC 100-22, Pasadena, CA 91125, USA

<sup>7</sup> Department of Physics and Astronomy, UCLA, Los Angeles, CA 90095, USA

<sup>8</sup> Infrared Processing and Analysis Center, California Institute of Technology, MC 100-22, Pasadena, CA 91125, USA

data. This result has been interpreted as the first detection of so-called “anomalous” dust emission outside of the Milky Way. Given that the excess was only detected for a single region, this emission component may be negligible for globally integrated measurements.

Due to the faintness of galaxies at high (i.e.,  $\gtrsim 15$  GHz) microwave frequencies, existing work has been restricted to the brightest objects, and small sample sizes. For example, past studies demonstrating the link between high-frequency free-free emission and massive star formation include investigations of Galactic star-forming regions (e.g., Mezger & Henderson 1967), nearby dwarf irregular galaxies (e.g., Klein & Graeve 1986), galaxy nuclei (e.g., Turner & Ho 1983, 1994), nearby starbursts (e.g., Klein et al. 1988; Turner & Ho 1985), and super star clusters within nearby blue compact dwarfs (e.g., Turner et al. 1998; Kobulnicky & Johnson 1999). And while these studies focus on the free-free emission from galaxies, each was conducted at frequencies  $\lesssim 30$  GHz. With recent improvements to the backends of existing radio telescopes, such as the Caltech Continuum Backend (CCB) on the Green Bank Telescope (GBT) and the Wideband Interferometric Digital ARchitecture (WIDAR) correlator on the Karl G. Jansky Very Large Array (VLA), the availability of increased bandwidth is making it possible to conduct investigations for large samples of objects at frequencies  $\sim 30$  GHz.

Here we present such an investigation using GBT 33 GHz photometry for 103 galaxy nuclei and extranuclear star-forming regions in a sample of 46 nearby galaxies included in the Star Formation in Radio Survey (SFRS; see §2.1). These galaxies, which are included in the *Spitzer* Infrared Nearby Galaxies Survey (SINGS; Kennicutt et al. 2003) and Key Insights on Nearby Galaxies: a Far-Infrared Survey with *Herschel* (KINGFISH; Kennicutt et al. 2011) legacy programs, are well studied and have a wealth of ancillary data available. We are currently in the process of collecting complementary interferometric observations of these same targets using the VLA, which will be presented in a forthcoming paper. This paper is organized as follows: In §2 we describe our sample selection and the data used in the present study. In §3 we describe our analysis procedures. Our results are presented in §4 and discussed in §5. Finally, in §6, we summarize our main conclusions.

## 2. SAMPLE AND DATA

In this section we describe the sample selection. We additionally present the GBT observations and provide a description of the ancillary data utilized for the present study.

### 2.1. Sample Selection

The Star Formation in Radio Survey (SFRS) sample comprises nuclear and extranuclear star-forming regions in 56 nearby galaxies ( $d < 30$  Mpc) observed as part of the SINGS (Kennicutt et al. 2003) and KINGFISH (Kennicutt et al. 2011) legacy programs. Each of these nuclear and extranuclear star-forming complexes have  $\sim 1' \times 0.5'$  sized mid-infrared (i.e., low resolution from  $5 - 14 \mu\text{m}$  and high resolution from  $10 - 37 \mu\text{m}$ ) spectral mappings carried out by the IRS instrument on board *Spitzer*, and  $47'' \times 47''$  sized *Herschel*/PACS far-infrared spectral mappings for a combination of the prin-

cipal atomic ISM cooling lines of [OI]63  $\mu\text{m}$ , [OIII]88  $\mu\text{m}$ , [NII]122,205  $\mu\text{m}$ , and [CII]158  $\mu\text{m}$ . Two galaxies that are exceptions include NGC 5194 and NGC 2403; these galaxies were part of the SINGS sample, but are not formally included in KINGFISH. They were observed with *Herschel* as part of the Very Nearby Galaxy Survey (VNGS; PI: C. Wilson). Similarly, there are additional KINGFISH galaxies that were not part of SINGS, but have existing *Spitzer* data: NGC 5457 (M 101), IC 342, NGC 3077, and NGC 2146.

SINGS and KINGFISH galaxies were chosen to cover the full range of integrated properties and ISM conditions found in the local Universe, spanning the full range in morphological types, a factor of  $\sim 10^5$  in infrared (IR:  $8 - 1000 \mu\text{m}$ ) luminosity, a factor of  $\sim 10^3$  in  $L_{\text{IR}}/L_{\text{opt}}$ , and a large range in star formation rate ( $\lesssim 10^{-3} - 10 M_{\odot} \text{yr}^{-1}$ ). Similarly, spectroscopically targeted extranuclear sources included in SINGS and KINGFISH were selected to cover the full range of physical conditions and spectral characteristics found in (bright) infrared sources in nearby galaxies, requiring optical and infrared selections. Optically selected extranuclear regions were chosen to span a large range in physical properties including extinction-corrected production rate of ionizing photons [ $Q(H^0) \sim 10^{49} - 10^{52} \text{s}^{-1}$ ], metallicity ( $\sim 0.1 - 3 Z_{\odot}$ ), visual extinction ( $A_V \lesssim 4 \text{mag}$ ), radiation field intensity (100-fold range), ionizing stellar temperature ( $T_{\text{eff}} \sim 3.5 - 5.5 \times 10^4 \text{K}$ ), and local  $\text{H}_2/\text{HI}$  ratios ( $\lesssim 0.1 - \gtrsim 10$ ). A sub-sample of infrared-selected extranuclear targets were chosen to span a range in  $f_{\nu}(8 \mu\text{m})/f_{\nu}(24 \mu\text{m})$  and  $f_{\text{H}\alpha}/f_{\nu}(8 \mu\text{m})$  ratios.

The total sample over the entire sky consists of 118 star-forming complexes (56 nuclei and 62 extranuclear regions), 103 of which (46 nuclei and 57 extranuclear regions; see Tables 1 and 2, respectively) are observable with the GBT (i.e., having  $\delta > -30^\circ$ ). Galaxy morphologies, adopted distances, and optically-defined nuclear types are given in Table 1. In Figure 1, we show the location of each target region on *Spitzer* 24  $\mu\text{m}$  images; the corresponding circle diameters are  $25''$ , which match the FWHM of our lowest resolution data (i.e., the beam of the GBT 33 GHz radio data) for the present multiwavelength study.

### 2.2. GBT Observations and Data Reduction

Observations in the Ka band (26 – 40 GHz) were taken using the Caltech Continuum Backend (CCB) on the 100 m Robert C. Byrd Green Bank Telescope (GBT; Jewell & Prestage 2004) over a two year period spanning 2009 March through 2011 January. The CCB simultaneously measures the entire Ka bandwidth over four equally spaced frequency channels (i.e., 27.75, 31.25, 34.75, and 38.25 GHz) and synchronously reads out and demodulates the beam-switched signal to remove atmospheric fluctuation and/or gain variations. The FWHM of the GBT beam across the full Ka band was typically  $\approx 25''$  among our sets of observations (see §3.1). Given the range of distances to the sample galaxies, this projects to linear scales of 0.37 – 3.7 kpc. Reference beams used for sky subtraction are measured by nodding  $1/3$  away from the source, and their positions are identified on top of *Spitzer* 24  $\mu\text{m}$  images in Figure 1.

Observations were made using an “On-the-Fly Nod”

**Table 1**  
Nuclear Source Positions and 33 GHz Photometry

Galaxy	R.A. (J2000)	Decl. (J2000)	Type <sup>a</sup>	Dist. <sup>b</sup> (Mpc)	Nuc. Type <sup>c</sup>	$S_{33\text{ GHz}}$ (mJy)	$S_{33\text{ GHz}}^d$ (mJy)
NGC 337	0 59 50.3	- 7 34 44	SBd	19.3	SF	$2.59 \pm 0.21$	...
NGC 628	1 36 41.7	+15 46 59	SAC	7.2	...	$0.11 \pm 0.03$	<0.09
NGC 855	2 14 3.7	+27 52 37	E	9.73	SF	$0.68 \pm 0.05$	...
NGC 925	2 27 17.0	+33 34 42	SABd	9.12	SF	$0.50 \pm 0.04$	...
NGC 1266	3 16 0.8	- 2 25 37	SB0	30.6	AGN	$8.45 \pm 0.45$	...
NGC 1377	3 36 38.9	-20 54 6	S0	24.6	...	< 0.44	...
IC 342	3 46 48.5	+68 5 45	SABcd	3.28	SF(*)	$25.39 \pm 1.27$	...
NGC 1482	3 54 39.5	-20 30 6	SA0	22.6	SF	$10.78 \pm 0.56$	...
NGC 2146	6 18 37.7	+78 21 24	Sbab	17.2	SF(*)	$76.16 \pm 3.83$	...
NGC 2403	7 36 50.0	+65 36 3	SABcd	3.22	SF(*)	$0.28 \pm 0.03$	$0.15 \pm 0.03$
Holmberg II	8 19 13.3	+70 43 8	Im	3.05	...	$0.69 \pm 0.04$	...
NGC 2798	9 17 22.8	+41 59 57	SBa	25.8	SF/AGN	$7.82 \pm 0.52$	...
NGC 2841	9 22 2.7	+50 58 36	SAB	14.1	AGN	$1.53 \pm 0.08$	...
NGC 2976	9 47 15.3	+67 55 0	SAC	3.55	SF	$0.49 \pm 0.07$	$0.29 \pm 0.07$
NGC 3049	9 54 49.6	+ 9 16 17	SBab	19.2	SF	$1.56 \pm 0.13$	...
NGC 3077	10 3 19.1	+68 44 2	IOpec	3.83	SF(*)	$7.55 \pm 0.40$	...
NGC 3190	10 18 5.6	+21 49 54	SAap	19.3	AGN(*)	$0.93 \pm 0.08$	...
NGC 3184	10 18 16.7	+41 25 27	SABcd	11.7	SF	< 0.18	...
NGC 3198	10 19 54.9	+45 32 58	SBc	14.1	SF	$0.72 \pm 0.11$	...
IC 2574	10 28 48.4	+68 28 1	SABm	3.79	SF(*)	$0.62 \pm 0.05$	...
NGC 3265	10 31 6.7	+28 47 48	E	19.6	SF	$1.05 \pm 0.14$	...
NGC 3351	10 43 57.8	+11 42 14	SBb	9.33	SF	$4.86 \pm 0.27$	...
NGC 3521	11 5 48.9	- 0 2 6	SABbc	11.2	SF/AGN(*)	$1.45 \pm 0.10$	...
NGC 3627	11 20 15.0	+12 59 30	SABb	9.38	AGN	$2.70 \pm 0.16$	...
NGC 3773	11 38 13.0	+12 6 45	SA0	12.4	SF	$0.95 \pm 0.07$	...
NGC 3938	11 52 49.5	+44 7 14	SAC	17.9	SF(*)	< 0.19	...
NGC 4254	12 18 49.4	+14 24 59	SAC	14.4	SF/AGN	$1.60 \pm 0.12$	...
NGC 4321	12 22 54.9	+15 49 21	SABbc	14.3	AGN	$4.34 \pm 0.24$	...
NGC 4536	12 34 27.1	+ 2 11 17	SABbc	14.5	SF/AGN	$17.49 \pm 0.88$	...
NGC 4559	12 35 57.7	+27 57 35	SABcd	6.98	SF	$0.70 \pm 0.05$	...
NGC 4569	12 36 49.8	+13 9 46	SABab	9.86	AGN	$1.81 \pm 0.13$	...
NGC 4579	12 37 43.6	+11 49 1	SABb	16.4	AGN	$23.38 \pm 1.17$	...
NGC 4594	12 39 59.4	-11 37 23	SAa	9.08	AGN	$69.30 \pm 3.47$	...
NGC 4625	12 41 52.4	+41 16 23	SABmp	9.3	SF	$0.36 \pm 0.02$	...
NGC 4631	12 42 5.9	+32 32 21	SBd	7.62	SF(*)	$3.83 \pm 0.21$	...
NGC 4725	12 50 26.6	+25 30 6	SABab	11.9	AGN	$0.29 \pm 0.03$	...
NGC 4736	12 50 53.0	+41 7 14	SAab	4.66	AGN(*)	$2.86 \pm 0.16$	...
NGC 4826	12 56 43.9	+21 40 59	SAab	5.27	AGN	$5.88 \pm 0.31$	...
NGC 5055	13 15 49.2	+42 1 49	SABc	7.94	AGN	$2.58 \pm 0.25$	...
NGC 5194	13 29 52.7	+47 11 43	SABbc	7.62	AGN	$6.25 \pm 0.39$	...
NGC 5457	14 3 12.6	+54 20 57	SABcd	6.7	SF(*)	< 0.73	...
NGC 5474	14 5 1.3	+53 39 43	SACd	6.8	SF(*)	$0.17 \pm 0.05$	$0.16 \pm 0.05$
NGC 5713	14 40 11.3	- 0 17 26	SABbc	21.4	SF	$6.34 \pm 0.35$	...
NGC 5866	15 6 29.5	+55 45 47	S0	15.3	AGN	$6.21 \pm 0.32$	...
NGC 6946	20 34 52.3	+60 9 14	SABcd	6.8	SF	$15.84 \pm 0.80$	...
NGC 7331	22 37 4.1	+34 24 56	SAB	14.5	AGN	$1.42 \pm 0.11$	...

<sup>a</sup> Morphological type taken from the NASA Extragalactic Database (NED; <http://nedwww.ipac.caltech.edu>).

<sup>b</sup> Redshift-independent distance taken from the list compiled by Kennicutt et al. (2011), except for the two non-KINGFISH galaxies NGC 5194 (Ciardullo et al. 2002) and NGC 2403 (Freedman et al. 2001).

<sup>c</sup> Nuclear Type based optical spectroscopy: SF = Star-Forming; AGN = Non-thermal emission as given in Table 5 of Moustakas et al. (2010) or (\*) Table 4 of Ho et al. (1997).

<sup>d</sup> Measured 33 GHz flux densities before applying a correction for the oversubtraction of emission due to reference nods falling on bright regions of the galaxy. Corrections were only applied to cases where the estimated loss is >15%.

variant of a symmetric nodding procedure (i.e., double-differencing technique; Readhead et al. 1989) with data being collected continuously through an entire observation, including slews between beams. This procedure alternately places the source of interest in each of the two beams of the Ka-band receiver in an A/B/B/A pattern. Such a sequence is able to cancel means and gradients in the atmospheric or receiver noise with time. Each nodding cycle lasts  $\approx 70$  s: an on-source dwell time of 10 s for each of the 4 phases, along with 10 s spent on the initial position acquisition, and 10 s for the 2 slews between beams. Thus,  $\approx 40$  s is spent on source per nodding cycle. A detailed description on the performance of the

CCB receiver, the data reduction pipeline, and error estimates is given in Mason et al. (2009). In addition to any systematic errors, we assign a calibration error of 10% to the flux density measurement at each frequency channel.

Our observing strategy was constructed to make the most efficient use of the telescope. Thus, given the large range in brightness among our targeted regions, we varied the time spent on source based on an estimate of the expected 33 GHz flux density using the *Spitzer* 24  $\mu$ m maps. The number of nods spent on each source was chosen to reach a S/N ratio of  $\approx 10$ , while never spending  $\lesssim 5$  min (i.e.,  $\approx 4$  nods) nor  $\gtrsim 70$  min (i.e.,  $\approx 60$  nods) of total integration time on a given source. Naturally, not

**Table 2**  
Extranuclear Source Positions and 33 GHz Photometry

ID	R.A. (J2000)	Decl. (J2000)	$S_{33 \text{ GHz}}$ (mJy)	$S_{33 \text{ GHz}}^a$ (mJy)
NGC 628 Enum. 1	1 36 45.1	+15 47 51	$0.54 \pm 0.17$	...
NGC 628 Enum. 2	1 36 37.5	+15 45 11	$0.35 \pm 0.04$	...
NGC 628 Enum. 3	1 36 38.8	+15 44 25	$0.54 \pm 0.04$	$0.46 \pm 0.04$
NGC 628 Enum. 4	1 36 35.5	+15 50 11	$0.23 \pm 0.05$	$< 0.16$
NGC 2403 Enum. 1	7 36 45.5	+65 37 0	$1.68 \pm 0.14$	...
NGC 2403 Enum. 2	7 36 52.7	+65 36 46	$1.33 \pm 0.13$	...
NGC 2403 Enum. 3	7 37 6.9	+65 36 38	$3.04 \pm 0.19$	...
NGC 2403 Enum. 4	7 37 17.9	+65 33 46	$1.37 \pm 0.08$	...
NGC 2403 Enum. 5	7 36 19.5	+65 37 4	$1.28 \pm 0.21$	...
NGC 2403 Enum. 6	7 36 28.5	+65 33 50	$0.73 \pm 0.06$	...
NGC 2976 Enum. 1	9 47 7.8	+67 55 51	$3.62 \pm 0.21$	...
NGC 2976 Enum. 2	9 47 24.1	+67 53 56	$2.12 \pm 0.15$	$1.92 \pm 0.15$
NGC 3521 Enum. 1	11 5 46.3	- 0 4 9	$0.47 \pm 0.02$	$0.25 \pm 0.02$
NGC 3521 Enum. 2	11 5 49.9	- 0 3 38	$0.90 \pm 0.09$	...
NGC 3521 Enum. 3	11 5 47.6	+ 0 0 33	$0.37 \pm 0.03$	...
NGC 3627 Enum. 1	11 20 16.2	+12 57 50	$2.42 \pm 0.15$	...
NGC 3627 Enum. 2	11 20 16.3	+12 58 44	$6.16 \pm 0.32$	...
NGC 3627 Enum. 3	11 20 16.0	+12 59 52	$0.77 \pm 0.08$	$0.62 \pm 0.08$
NGC 3938 Enum. 1	11 52 46.4	+44 7 0	$0.15 \pm 0.02$	$0.10 \pm 0.02$
NGC 3938 Enum. 2	11 53 0.0	+44 7 54	$< 0.66$	...
NGC 4254 Enum. 1	12 18 49.1	+14 23 58	$1.10 \pm 0.08$	...
NGC 4254 Enum. 2	12 18 44.6	+14 24 24	$0.19 \pm 0.04$	$< 0.13$
NGC 4321 Enum. 1	12 22 58.9	+15 49 35	$0.15 \pm 0.05$	$< 0.14$
NGC 4321 Enum. 2	12 22 49.8	+15 50 29	$0.16 \pm 0.04$	$< 0.13$
NGC 4631 Enum. 1	12 41 40.8	+32 31 50	$0.90 \pm 0.08$	...
NGC 4631 Enum. 2	12 42 21.3	+32 33 6	$0.67 \pm 0.06$	...
NGC 4736 Enum. 1	12 50 56.2	+41 7 19	$2.58 \pm 0.15$	...
NGC 5055 Enum. 1	13 15 58.0	+42 0 25	$0.43 \pm 0.12$	$< 0.37$
NGC 5194 Enum. 1	13 29 53.1	+47 12 39	$< 0.87$	...
NGC 5194 Enum. 2	13 29 44.1	+47 10 21	$1.72 \pm 0.24$	...
NGC 5194 Enum. 3	13 29 44.6	+47 9 55	$1.00 \pm 0.23$	...
NGC 5194 Enum. 4	13 29 56.2	+47 14 7	$2.06 \pm 0.23$	$1.77 \pm 0.23$
NGC 5194 Enum. 5	13 29 59.6	+47 14 0	$2.05 \pm 0.24$	$1.82 \pm 0.24$
NGC 5194 Enum. 6	13 29 39.5	+47 8 35	$0.92 \pm 0.07$	$0.85 \pm 0.07$
NGC 5194 Enum. 7	13 30 2.5	+47 9 51	$< 0.64$	...
NGC 5194 Enum. 8	13 30 1.6	+47 12 51	$0.97 \pm 0.27$	...
NGC 5194 Enum. 9	13 29 59.9	+47 11 12	$1.03 \pm 0.22$	$0.78 \pm 0.22$
NGC 5194 Enum. 10	13 29 56.7	+47 10 45	$0.85 \pm 0.22$	$< 0.66$
NGC 5194 Enum. 11	13 29 49.7	+47 13 28	$0.69 \pm 0.10$	$< 0.30$
NGC 5457 Enum. 1	14 3 10.2	+54 20 57	$0.39 \pm 0.12$	...
NGC 5457 Enum. 2	14 2 55.0	+54 22 26	$0.29 \pm 0.08$	...
NGC 5457 Enum. 3	14 3 41.3	+54 19 4	$8.27 \pm 0.52$	...
NGC 5457 Enum. 4	14 3 53.1	+54 22 5	$2.11 \pm 0.22$	...
NGC 5457 Enum. 5	14 3 1.1	+54 14 27	$2.49 \pm 0.27$	...
NGC 5457 Enum. 6	14 2 28.1	+54 16 26	$3.38 \pm 0.33$	...
NGC 5457 Enum. 7	14 4 29.3	+54 23 45	$4.69 \pm 0.35$	...
NGC 5713 Enum. 1	14 40 12.1	- 0 17 47	$1.18 \pm 0.14$	...
NGC 5713 Enum. 2	14 40 10.5	- 0 17 47	$1.48 \pm 0.15$	...
NGC 6946 Enum. 1	20 35 16.7	+60 11 0	$0.74 \pm 0.05$	$0.39 \pm 0.05$
NGC 6946 Enum. 2	20 35 25.5	+60 10 1	$2.36 \pm 0.16$	...
NGC 6946 Enum. 3	20 34 51.9	+60 12 45	$1.01 \pm 0.07$	...
NGC 6946 Enum. 4	20 34 19.2	+60 10 9	$3.01 \pm 0.15$	$2.89 \pm 0.15$
NGC 6946 Enum. 5	20 34 39.3	+60 4 54	$0.51 \pm 0.04$	...
NGC 6946 Enum. 6	20 35 6.1	+60 11 0	$2.86 \pm 0.18$	...
NGC 6946 Enum. 7	20 35 11.2	+60 9 0	$3.20 \pm 0.20$	...
NGC 6946 Enum. 8	20 34 32.5	+60 10 22	$1.80 \pm 0.14$	...
NGC 6946 Enum. 9	20 35 12.7	+60 8 53	$2.49 \pm 0.17$	...

<sup>a</sup> Measured 33 GHz flux densities before applying a correction for the over-subtraction of emission due to reference nodes falling on bright regions of the galaxy. Corrections were only applied to cases where the estimated loss is  $> 15\%$ .

all nods were deemed usable given weather conditions and technical difficulties, and sources were revisited if possible. We list the number of nods used and taken, along with the corresponding time spent on source, for the nuclear and extranuclear regions in Appendix Tables 6 and 7, respectively.

### 2.3. Ancillary UV, Optical, Infrared, and Radio Data

*Galaxy Evolution Explorer (GALEX)* far-UV (FUV; 1528 Å) and near-UV (NUV; 2271 Å) data were taken from the *GALEX* archive (GR6) and will be included in the *GALEX* Large Galaxy Atlas (M. Seibert et al. 2012, in preparation). We also made use of star masks generated by the *GALEX* team to identify and remove foreground stars for the analysis. The angular resolutions of the FUV and NUV images are 4".25 and 5".25, respectively, while the calibration uncertainty for these data is  $\approx 15\%$  in both bands.

The H $\alpha$  imaging used in the analysis is taken from Leroy et al. (2012), where details about the data quality and preparation (e.g., correction for [NII] emission) can be found. Like the UV data, H $\alpha$  images were corrected for foreground stars. The typical resolution of the H $\alpha$  images is  $\approx 2''$ , and the calibration uncertainty among these maps is taken to be  $\approx 20\%$ .

Archival *Spitzer* 24  $\mu$ m data were largely taken from the SINGS and Local Volume Legacy (LVL) legacy programs, and have a calibration uncertainty of  $\approx 5\%$ . Details on the associated observation strategies and data reduction steps can be found in Dale et al. (2007) and Dale et al. (2009), respectively. Two galaxies, IC 342 and NGC 2146, were not a part of SINGS or LVL; their 24  $\mu$ m imaging comes from Engelbracht et al. (2008).

We additionally made use of *Herschel* 70, 100, 160, and 250  $\mu$ m data from KINGFISH (see Kennicutt et al. 2011). Observations with the PACS instrument (Poglitsch et al. 2010) were carried out at 70, 100, and 160  $\mu$ m in the Scan-Map mode and reduced by the Scanamorphos data reduction pipeline, version 12.5 (Roussel 2012). The goal of the Scanamorphos reduction is to preserve low-surface-brightness emission. The 250  $\mu$ m observations were made using the SPIRE instrument (Griffin et al. 2010) and reduced using the HIPE version spire-5.0.1894. For NGC 2403 and NGC 5194, we make use of *Herschel* 70, 160, and 250  $\mu$ m imaging obtained as part of the VNGS program. Information on the observational strategy and data processing can be found in Bendo et al. (2011) for NGC 2403 and E. Mentuch (2012, in preparation) for NGC 5194.

Ancillary radio data at 1.365 and 1.697 GHz for 24 of the sample galaxies are available from the Westerbork Synthesis Radio Telescope SINGS survey (Braun et al. 2007). The intrinsic FWHM of the radio beams is approximately 11" east-west by 11/sin  $\delta''$  north-south at 1.5 GHz and scales as wavelength, where  $\delta$  is the source declination. For 5 galaxies (i.e., NGC 628, NGC 3627, NGC 4254, NGC 4321, NGC 4569) the north-south axis of the WSRT-SINGS beam at 1.7 GHz is larger than median FWHM of the 33 GHz GBT beam (including the 1  $\sigma$  scatter), ranging between 36".5 and 44". Similarly, for 7 galaxies (i.e., NGC 628, NGC 3627, NGC 4254, NGC 4321, NGC 4569, and NGC 4725, and NGC 4826) the north-south axis of the WSRT-SINGS beam at

1.4 GHz is larger than the median +1 $\sigma$  scatter on the 33 GHz GBT beam, ranging between 29" and 55".5. Since this will affect the accuracy of the matched photometry with the GBT 33 GHz data, we do not include these sources in the radio spectral index analysis. The flux density calibration of the radio maps is better than  $\approx 5\%$ .

## 3. PHOTOMETRY AND ANALYSIS

In the following section we describe our procedure to produce resolution-matched photometry among all data sets. Special considerations when dealing with the GBT single-beam photometry are also described in detail.

We also note that the beam of the GBT averages over significantly large physical areas given the distances of the sample galaxies (e.g., as large as  $\sim 3.7$  kpc with a median linear scale of  $\approx 0.9$  kpc among all nuclei and extranuclear sources targeted), and likely contains a number of non-coeval HII regions, photodissociation regions, and diffuse emission. This is similar to the physical scale of  $\approx 0.8$  kpc investigated by Murphy et al. (2011), who found that conducting their analysis with and without local background subtractions did not qualitatively affect their main conclusions. We therefore do not attempt to subtract local background estimates, which would add more uncertainty to the present analysis.

### 3.1. GBT Observations: Additional Considerations

Among all sets of observations, we measure a median beam width over all channels of 25".07 with a dispersion of 3".1. However, given that we are targeting resolved sources, and the beam size varies over the full Ka band, we apply a correction to the flux densities at each frequency channel as if their beam were at the nominal 25". We use the scaling factors given in Murphy et al. (2010), since the distance to NGC 6946 is close to the median distance among the entire SFRS sample. These scale factors were derived by computing the photometry for NGC 6946 on the 8.5 GHz map using the beam sizes for each frequency channel averaged over that entire observing session, and are 0.89, 0.95, 1.00, and 1.04 at 27.75, 31.25, 34.75, and 38.25 GHz, respectively. While the exact values of these corrections factors will change depending on source geometry/morphology, the final 33 GHz photometry, averaged over the entire band, should be robust. The combination of resolved sources and the changing beam size across the Ka band will complicate the interpretation of in-band radio spectral indices, and is therefore not presented.

While the unblocked aperture and active surface of the GBT mitigate the significance of sidelobes, we inspected calibration scans from each observing session to determine if there were instances of days exhibiting sidelobes with large amplitudes. The added power may cause an overestimation of the 33 GHz flux density. We find that sidelobes, when measurable, have an amplitude that is  $\lesssim 2\%$  of the beam peak, on average, over the entire 2 year observing campaign. At this level, our results should not be significantly affected by the presence of sidelobes given that Murphy et al. (2010) found negligible differences in their ancillary radio, submillimeter, and infrared photometry using a model beam having sidelobes at 5% of the beam peak.

The averaged Ka-band flux densities, weighted by the errors from each channel over the full band, are given

**Table 3**  
Nuclear Photometry from Ancillary Data

Galaxy	$f_\nu(24\ \mu\text{m})$ (mJy)	$F_{\text{IR}}/10^{-11}$ ( $\text{erg s}^{-1}\text{ cm}^{-2}$ )	$S_{1.7\text{GHz}}$ (mJy)	$S_{1.4\text{GHz}}$ (mJy)	$f_\nu(1528\ \text{\AA})$ (mJy)	$f_\nu(2271\ \text{\AA})$ (mJy)	$f_{\text{H}\alpha}/10^{-13}$ ( $\text{erg s}^{-1}\text{ cm}^{-2}$ )	$E(B-V)^a$ (mag)
NGC 337	241.0 ± 42.7	23.6 ± 4.2	...	...	1.7 ± 0.4	3.8 ± 0.9	8.3 ± 2.2	0.112
NGC 628	57.4 ± 10.2	8.3 ± 1.6	...	...	...	...	...	0.070
NGC 855	60.8 ± 10.8	7.6 ± 1.5	...	...	1.0 ± 0.2	1.6 ± 0.4	...	0.071
NGC 925	46.2 ± 8.2	7.3 ± 1.3	1.8 ± 0.3	2.1 ± 0.4	2.2 ± 0.5	3.0 ± 0.7	3.6 ± 0.9	0.076
NGC 1266	811.6 ± 143.8	75.2 ± 27.7	...	...	0.02 ± 0.00	0.14 ± 0.03	...	0.098
NGC 1377	1804.0 ± 319.7	64.0 ± 11.7	...	...	...	...	...	0.028
IC 342	9561.4 ± 1694.3	584.5 ± 320.8	...	...	19.6 ± 4.4	119.4 ± 27.1	...	0.559
NGC 1482	1116.7 ± 197.9	152.8 ± 37.7	...	...	0.09 ± 0.02	0.3 ± 0.1	...	0.040
NGC 2146	7414.2 ± 1313.8	892.0 ± 164.1	504.3 ± 89.4	584.1 ± 103.5	0.16 ± 0.04	0.5 ± 0.1	...	0.096
NGC 2403	59.9 ± 10.6	11.3 ± 2.3	1.4 ± 0.2	1.8 ± 0.3	1.5 ± 0.3	2.5 ± 0.6	2.7 ± 0.7	0.040
Holmberg II	35.2 ± 6.2	1.8 ± 0.3	1.0 ± 0.2	1.2 ± 0.2	...	...	...	0.032
NGC 2798	956.1 ± 169.4	120.7 ± 22.7	...	...	...	...	...	0.020
NGC 2841	44.9 ± 8.0	4.4 ± 0.9	3.7 ± 0.7	4.4 ± 0.8	0.6 ± 0.1	1.0 ± 0.2	1.0 ± 0.3	0.015
NGC 2976	93.6 ± 16.6	10.1 ± 2.0	1.9 ± 0.3	2.1 ± 0.4	1.2 ± 0.3	2.0 ± 0.5	4.4 ± 1.2	0.072
NGC 3049	387.3 ± 68.6	20.6 ± 3.9	...	...	1.3 ± 0.3	2.2 ± 0.5	3.9 ± 1.0	0.038
NGC 3077	868.6 ± 153.9	72.5 ± 12.5	...	...	...	...	21.8 ± 5.7	0.067
NGC 3190	108.5 ± 19.2	22.7 ± 4.0	...	...	0.07 ± 0.01	0.3 ± 0.1	0.4 ± 0.1	0.025
NGC 3184	129.7 ± 23.0	11.6 ± 2.0	2.1 ± 0.4	2.3 ± 0.4	0.4 ± 0.1	0.9 ± 0.2	0.8 ± 0.2	0.017
NGC 3198	364.6 ± 64.6	20.8 ± 3.6	2.9 ± 0.5	3.2 ± 0.6	0.2 ± 0.1	0.4 ± 0.1	0.7 ± 0.2	0.012
IC 2574	41.2 ± 7.3	3.0 ± 0.5	0.7 ± 0.1	0.9 ± 0.2	1.0 ± 0.2	1.2 ± 0.3	4.3 ± 1.1	0.037
NGC 3265	278.8 ± 49.4	18.4 ± 3.2	...	...	0.4 ± 0.1	0.8 ± 0.2	...	0.024
NGC 3351	1435.0 ± 254.3	103.7 ± 23.1	...	...	2.0 ± 0.4	5.3 ± 1.2	11.8 ± 3.1	0.028
NGC 3521	287.3 ± 50.9	37.9 ± 9.0	...	...	0.5 ± 0.1	2.0 ± 0.4	5.7 ± 1.5	0.057
NGC 3627	633.2 ± 112.2	90.4 ± 16.2	...	...	0.5 ± 0.1	1.7 ± 0.4	4.9 ± 1.3	0.033
NGC 3773	128.0 ± 22.7	9.4 ± 1.8	...	...	3.2 ± 0.7	4.0 ± 0.9	...	0.027
NGC 3938	68.2 ± 12.1	11.3 ± 2.1	1.3 ± 0.2	1.5 ± 0.3	0.7 ± 0.2	1.4 ± 0.3	1.2 ± 0.3	0.021
NGC 4254	436.0 ± 77.3	54.8 ± 16.2	...	...	1.1 ± 0.2	3.1 ± 0.7	6.4 ± 1.7	0.039
NGC 4321	723.2 ± 128.2	76.6 ± 14.3	...	...	2.4 ± 0.5	5.6 ± 1.3	6.3 ± 1.7	0.026
NGC 4536	2474.1 ± 438.4	193.3 ± 33.2	...	...	0.3 ± 0.1	0.7 ± 0.2	7.0 ± 1.8	0.018
NGC 4559	84.2 ± 14.9	12.0 ± 2.0	2.5 ± 0.4	3.0 ± 0.5	1.2 ± 0.3	1.9 ± 0.4	4.0 ± 1.0	0.018
NGC 4569	701.4 ± 124.3	47.3 ± 9.5	...	...	0.9 ± 0.2	3.3 ± 0.8	8.9 ± 2.3	0.047
NGC 4579	170.7 ± 30.2	15.5 ± 2.7	...	...	0.3 ± 0.1	0.8 ± 0.2	5.3 ± 1.4	0.041
NGC 4594	110.9 ± 19.6	7.9 ± 1.6	...	...	0.6 ± 0.1	1.5 ± 0.3	...	0.051
NGC 4625	45.4 ± 8.1	6.4 ± 1.2	...	...	1.1 ± 0.2	1.6 ± 0.4	1.7 ± 0.5	0.018
NGC 4631	566.5 ± 100.4	79.2 ± 13.9	39.9 ± 7.1	45.8 ± 8.1	1.6 ± 0.4	2.4 ± 0.6	4.8 ± 1.3	0.017
NGC 4725	54.2 ± 9.6	4.4 ± 0.8	0.3 ± 0.0	...	0.17 ± 0.04	0.4 ± 0.1	0.3 ± 0.1	0.012
NGC 4736	1094.8 ± 194.0	150.4 ± 33.1	23.8 ± 4.2	24.8 ± 4.4	1.7 ± 0.4	5.8 ± 1.3	4.9 ± 1.3	0.018
NGC 4826	1088.9 ± 193.0	167.6 ± 30.5	33.9 ± 6.0	...	1.0 ± 0.2	2.7 ± 0.6	17.1 ± 4.5	0.041
NGC 5055	353.0 ± 62.6	76.8 ± 13.6	18.1 ± 3.2	20.6 ± 3.7	0.6 ± 0.1	1.9 ± 0.4	5.8 ± 1.5	0.018
NGC 5194	608.9 ± 107.9	95.2 ± 26.0	52.2 ± 9.3	58.5 ± 10.4	2.2 ± 0.5	6.1 ± 1.4	11.1 ± 2.9	0.035
NGC 5457	177.7 ± 31.5	20.6 ± 3.7	...	...	0.9 ± 0.2	1.9 ± 0.4	2.0 ± 0.5	0.009
NGC 5474	14.4 ± 2.6	2.5 ± 0.5	...	...	1.2 ± 0.3	1.5 ± 0.3	1.7 ± 0.5	0.010
NGC 5713	1137.6 ± 201.6	85.6 ± 16.6	...	...	1.7 ± 0.4	3.6 ± 0.8	5.6 ± 1.5	0.039
NGC 5866	95.5 ± 16.9	33.8 ± 5.9	...	...	0.12 ± 0.03	0.6 ± 0.1	...	0.013
NGC 6946	4355.3 ± 771.8	301.0 ± 60.0	83.8 ± 14.8	91.9 ± 16.3	0.4 ± 0.1	2.0 ± 0.5	18.1 ± 4.8	0.343
NGC 7331	301.9 ± 53.5	49.0 ± 8.6	17.2 ± 3.0	20.1 ± 3.6	0.3 ± 0.1	1.6 ± 0.4	2.3 ± 0.6	0.091

<sup>a</sup> Galactic extinction taken from (Schlegel et al. 1998) used to correct the H $\alpha$  and GALEX FUV and NUV flux densities assuming  $A_V/E(B-V) = 3.1$  and the modeled extinction curves of Weingartner & Draine (2001); Draine (2003).

in Tables 1 and 2 along with uncertainties; the corresponding effective frequency is given for each source in Appendix Tables 6 and 7, and is  $\approx 33$  GHz for each position (i.e., a median of 32.92 GHz with a dispersion of 0.79 GHz, corresponding to a  $\approx 2\%$  scatter in flux densities assuming a spectral index near 33 GHz of  $\sim 0.5$ ). For sources not detected at the  $3\sigma$  level, we list the  $3\sigma$  upper limit. Flux densities of the individual channels, *before applying any corrections*, are given with  $1\sigma$  errors in the Appendix Tables 6 and 7 for the galaxy nuclei and extranuclear regions, respectively. We do not give upper limits for the individual channels, but rather list the actual measured values and estimated errors.

Since the reference beam throw is only  $1'.3$ , real signal in our reference positions is a concern; having reference positions on the galaxy may result in an underestimation of the 33 GHz flux density (see Figure 1). For NGC 6946, we note that the positions presented here correct those

originally given in Murphy et al. (2010), however this slight correction does not impact their results. To quantitatively assess the severity of having real signal in the reference beam for our measurement, we estimate over-subtractions using the  $24\ \mu\text{m}$  data by comparing the flux densities measured at the reference positions compared to the on-source position. To correct for these losses, we add back to the 33 GHz flux densities the average flux densities measured among the reference positions using modeled 33 GHz maps by scaling the  $24\ \mu\text{m}$  data using Equation 2 of Murphy et al. (2006b). The minimum flux density of the reference beam positions for each target was then taken as the local sky and subtracted.

These corrections are typically small, having a median value of  $\approx 2\%$  among all sources. We conservatively apply corrections to only those 22 sources estimated to be missing  $>15\%$  of the actual flux density based on the  $24\ \mu\text{m}$  photometry alone. The median correction to the 33 GHz

**Table 4**  
Extranuclear Photometry from Ancillary Data

Galaxy	$f_\nu(24\ \mu\text{m})$ (mJy)	$F_{\text{IR}}/10^{-11}$ ( $\text{erg s}^{-1}\ \text{cm}^{-2}$ )	$S_{1.7\text{GHz}}$ (mJy)	$S_{1.4\text{GHz}}$ (mJy)	$f_\nu(1528\ \text{\AA})$ (mJy)	$f_\nu(2271\ \text{\AA})$ (mJy)	$f_{\text{H}\alpha}/10^{-13}$ ( $\text{erg s}^{-1}\ \text{cm}^{-2}$ )	$E(B - V)^a$ (mag)
NGC 628 Enuc. 1	167.5 ± 29.7	10.0 ± 1.8	...	...	0.6 ± 0.1	0.9 ± 0.2	2.2 ± 0.6	0.070
NGC 628 Enuc. 2	87.9 ± 15.6	5.5 ± 1.0	...	...	0.5 ± 0.1	0.7 ± 0.2	1.3 ± 0.3	0.070
NGC 628 Enuc. 3	86.2 ± 15.3	6.4 ± 1.1	...	...	1.5 ± 0.3	2.0 ± 0.4	2.4 ± 0.6	0.070
NGC 628 Enuc. 4	25.8 ± 4.6	2.1 ± 0.4	...	...	0.4 ± 0.1	0.5 ± 0.1	1.2 ± 0.3	0.072
NGC 2403 Enuc. 1	247.5 ± 43.9	20.5 ± 3.8	4.3 ± 0.8	4.7 ± 0.8	6.4 ± 1.5	8.2 ± 1.9	13.3 ± 3.5	0.040
NGC 2403 Enuc. 2	189.3 ± 33.5	18.3 ± 5.0	3.7 ± 0.6	4.0 ± 0.7	3.7 ± 0.8	4.9 ± 1.1	10.0 ± 2.6	0.040
NGC 2403 Enuc. 3	808.9 ± 143.3	45.8 ± 10.5	9.6 ± 1.7	9.9 ± 1.8	5.9 ± 1.3	7.0 ± 1.6	21.6 ± 5.7	0.040
NGC 2403 Enuc. 4	68.8 ± 12.2	7.9 ± 1.4	2.2 ± 0.4	2.5 ± 0.4	1.1 ± 0.3	1.4 ± 0.3	3.4 ± 0.9	0.040
NGC 2403 Enuc. 5	171.3 ± 30.4	14.0 ± 2.5	3.6 ± 0.6	3.9 ± 0.7	4.4 ± 1.0	4.8 ± 1.1	10.3 ± 2.7	0.040
NGC 2403 Enuc. 6	27.7 ± 4.9	3.3 ± 0.6	1.5 ± 0.3	1.8 ± 0.3	1.2 ± 0.3	1.4 ± 0.3	3.8 ± 1.0	0.040
NGC 2976 Enuc. 1	411.4 ± 72.9	32.8 ± 7.4	5.8 ± 1.0	6.0 ± 1.1	1.3 ± 0.3	2.1 ± 0.5	15.1 ± 4.0	0.070
NGC 2976 Enuc. 2	186.5 ± 33.1	18.8 ± 3.5	3.2 ± 0.6	3.3 ± 0.6	1.2 ± 0.3	1.6 ± 0.4	8.8 ± 2.3	0.072
NGC 3521 Enuc. 1	23.8 ± 4.2	2.2 ± 0.4	...	...	0.17 ± 0.04	0.2 ± 0.1	0.8 ± 0.2	0.057
NGC 3521 Enuc. 2	138.9 ± 24.6	19.7 ± 3.6	...	...	0.2 ± 0.1	0.5 ± 0.1	2.0 ± 0.5	0.057
NGC 3521 Enuc. 3	30.3 ± 5.4	3.7 ± 0.7	...	...	0.20 ± 0.05	0.3 ± 0.1	0.7 ± 0.2	0.059
NGC 3627 Enuc. 1	405.9 ± 71.9	32.6 ± 5.8	...	...	0.3 ± 0.1	0.5 ± 0.1	2.5 ± 0.7	0.035
NGC 3627 Enuc. 2	1389.2 ± 246.2	111.7 ± 19.2	...	...	1.1 ± 0.3	2.5 ± 0.6	7.3 ± 1.9	0.033
NGC 3627 Enuc. 3	139.3 ± 24.7	19.6 ± 3.4	...	...	1.8 ± 0.4	3.4 ± 0.8	3.0 ± 0.8	0.033
NGC 3938 Enuc. 1	46.8 ± 8.3	6.2 ± 1.1	1.4 ± 0.2	1.7 ± 0.3	0.7 ± 0.2	1.0 ± 0.2	1.1 ± 0.3	0.021
NGC 3938 Enuc. 2	57.4 ± 10.2	3.4 ± 0.6	0.9 ± 0.2	0.9 ± 0.2	0.5 ± 0.1	0.6 ± 0.1	1.4 ± 0.4	0.021
NGC 4254 Enuc. 1	114.4 ± 20.3	10.0 ± 2.4	...	...	0.7 ± 0.2	1.2 ± 0.3	2.4 ± 0.6	0.039
NGC 4254 Enuc. 2	49.7 ± 8.8	6.5 ± 1.3	...	...	0.5 ± 0.1	0.8 ± 0.2	1.3 ± 0.4	0.039
NGC 4321 Enuc. 1	54.9 ± 9.7	7.1 ± 1.3	...	...	0.4 ± 0.1	0.8 ± 0.2	1.0 ± 0.3	0.026
NGC 4321 Enuc. 2	47.8 ± 8.5	6.5 ± 1.2	...	...	0.7 ± 0.2	1.1 ± 0.3	1.1 ± 0.3	0.026
NGC 4631 Enuc. 1	46.8 ± 8.3	6.3 ± 1.1	4.4 ± 0.8	4.8 ± 0.8	2.0 ± 0.5	2.6 ± 0.6	4.5 ± 1.2	0.018
NGC 4631 Enuc. 2	84.7 ± 15.0	8.8 ± 1.6	6.0 ± 1.1	6.8 ± 1.2	1.3 ± 0.3	1.6 ± 0.4	3.9 ± 1.0	0.017
NGC 4736 Enuc. 1	506.4 ± 89.7	54.4 ± 9.8	14.0 ± 2.5	14.2 ± 2.5	4.1 ± 0.9	5.7 ± 1.3	7.0 ± 1.8	0.018
NGC 5055 Enuc. 1	78.3 ± 13.9	8.0 ± 1.4	2.4 ± 0.4	2.9 ± 0.5	0.4 ± 0.1	0.6 ± 0.1	2.2 ± 0.6	0.018
NGC 5194 Enuc. 1	250.9 ± 44.5	29.1 ± 8.8	12.1 ± 2.2	14.0 ± 2.5	0.8 ± 0.2	1.7 ± 0.4	5.0 ± 1.3	0.035
NGC 5194 Enuc. 2	299.9 ± 53.1	37.4 ± 11.4	7.4 ± 1.3	8.4 ± 1.5	1.7 ± 0.4	2.9 ± 0.6	5.6 ± 1.5	0.036
NGC 5194 Enuc. 3	227.1 ± 40.2	22.8 ± 6.2	7.6 ± 1.3	8.4 ± 1.5	2.1 ± 0.5	3.4 ± 0.8	4.8 ± 1.3	0.036
NGC 5194 Enuc. 4	168.5 ± 29.9	21.1 ± 4.1	9.6 ± 1.7	11.0 ± 1.9	1.1 ± 0.2	1.7 ± 0.4	0.3 ± 0.1	0.035
NGC 5194 Enuc. 5	196.5 ± 34.8	23.2 ± 4.5	9.2 ± 1.6	10.5 ± 1.9	2.1 ± 0.5	3.4 ± 0.8	0.4 ± 0.1	0.035
NGC 5194 Enuc. 6	66.9 ± 11.9	8.1 ± 1.6	2.7 ± 0.5	3.1 ± 0.6	0.3 ± 0.1	0.4 ± 0.1	1.9 ± 0.5	0.038
NGC 5194 Enuc. 7	180.8 ± 32.0	17.0 ± 3.3	4.7 ± 0.8	5.3 ± 0.9	1.2 ± 0.3	1.8 ± 0.4	5.0 ± 1.3	0.036
NGC 5194 Enuc. 8	327.5 ± 58.0	31.2 ± 9.0	10.7 ± 1.9	11.8 ± 2.1	2.3 ± 0.5	3.5 ± 0.8	4.8 ± 1.2	0.035
NGC 5194 Enuc. 9	146.1 ± 25.9	17.3 ± 3.2	5.5 ± 1.0	6.0 ± 1.1	1.3 ± 0.3	2.3 ± 0.5	2.2 ± 0.6	0.035
NGC 5194 Enuc. 10	175.7 ± 31.1	24.4 ± 5.9	9.1 ± 1.6	10.4 ± 1.8	1.0 ± 0.2	1.8 ± 0.4	2.5 ± 0.7	0.036
NGC 5194 Enuc. 11	78.4 ± 13.9	9.8 ± 2.3	6.1 ± 1.1	7.3 ± 1.3	0.7 ± 0.2	1.2 ± 0.3	1.3 ± 0.4	0.035
NGC 5457 Enuc. 1	97.8 ± 17.3	12.3 ± 2.3	...	...	0.6 ± 0.1	1.1 ± 0.2	1.3 ± 0.3	0.009
NGC 5457 Enuc. 2	60.8 ± 10.8	5.4 ± 0.9	...	...	0.8 ± 0.2	1.0 ± 0.2	2.3 ± 0.6	0.009
NGC 5457 Enuc. 3	1279.4 ± 226.7	50.2 ± 9.9	...	...	2.9 ± 0.6	3.5 ± 0.8	19.6 ± 5.1	0.009
NGC 5457 Enuc. 4	143.3 ± 25.4	10.9 ± 1.9	...	...	3.8 ± 0.9	4.2 ± 1.0	8.0 ± 2.1	0.009
NGC 5457 Enuc. 5	186.6 ± 33.1	10.9 ± 2.2	...	...	2.9 ± 0.7	3.3 ± 0.8	10.0 ± 2.6	0.009
NGC 5457 Enuc. 6	248.0 ± 43.9	17.8 ± 3.3	...	...	3.9 ± 0.9	4.3 ± 1.0	10.5 ± 2.8	0.009
NGC 5457 Enuc. 7	162.7 ± 28.8	8.1 ± 1.9	...	...	...	...	...	0.010
NGC 5713 Enuc. 1	97.8 ± 17.3	14.2 ± 2.7	...	...	0.4 ± 0.1	1.0 ± 0.2	1.1 ± 0.3	0.039
NGC 5713 Enuc. 2	248.6 ± 44.1	20.3 ± 3.7	...	...	0.6 ± 0.1	1.2 ± 0.3	2.2 ± 0.6	0.039
NGC 6946 Enuc. 1	129.4 ± 22.9	11.5 ± 2.0	3.7 ± 0.7	4.3 ± 0.8	2.2 ± 0.5	4.7 ± 1.1	10.5 ± 2.8	0.342
NGC 6946 Enuc. 2	211.9 ± 37.5	16.3 ± 2.9	6.5 ± 1.2	7.4 ± 1.3	6.2 ± 1.4	11.4 ± 2.6	31.4 ± 8.2	0.344
NGC 6946 Enuc. 3	92.6 ± 16.4	10.1 ± 1.8	3.4 ± 0.6	3.8 ± 0.7	2.4 ± 0.6	4.7 ± 1.1	13.7 ± 3.6	0.342
NGC 6946 Enuc. 4	102.2 ± 18.1	10.3 ± 1.8	3.3 ± 0.6	3.8 ± 0.7	1.9 ± 0.4	4.1 ± 0.9	...	0.343
NGC 6946 Enuc. 5	36.4 ± 6.5	4.7 ± 0.8	2.2 ± 0.4	2.7 ± 0.5	1.4 ± 0.3	3.0 ± 0.7	8.9 ± 2.3	0.338
NGC 6946 Enuc. 6	445.3 ± 78.9	41.8 ± 7.4	11.8 ± 2.1	13.0 ± 2.3	2.9 ± 0.7	6.6 ± 1.5	23.2 ± 6.1	0.342
NGC 6946 Enuc. 7	454.0 ± 80.4	43.5 ± 7.6	9.8 ± 1.7	10.9 ± 1.9	2.5 ± 0.6	5.9 ± 1.3	22.3 ± 5.9	0.342
NGC 6946 Enuc. 8	233.4 ± 41.4	24.1 ± 4.3	6.5 ± 1.1	7.5 ± 1.3	...	...	...	0.343
NGC 6946 Enuc. 9	367.6 ± 65.1	36.8 ± 6.7	8.5 ± 1.5	9.6 ± 1.7	1.7 ± 0.4	4.1 ± 0.9	14.2 ± 3.7	0.342

<sup>a</sup> Galactic extinction taken from (Schlegel et al. 1998) used to correct the H $\alpha$  and GALEX FUV and NUV flux densities assuming  $A_V/E(B - V) = 3.1$  and the modeled extinction curves of Weingartner & Draine (2001); Draine (2003).

flux density for these sources is  $\approx 24\%$ . The uncorrected 33 GHz flux densities are given in the final columns of Tables 1 and 2. We note that for the case of NGC 6946, using 8.5 GHz-derived 33 GHz maps resulted in corrections that agreed to those based on the 24  $\mu\text{m}$ -derived values to within a few percent (Murphy et al. 2010).

### 3.2. Ancillary Data

The photometry was carried out on the ancillary data sets after matching their resolution, cropping each image

to a common field-of-view, and re-gridding to a common pixel scale. To accurately match the photometry from these images to the GBT measurements, maps were convolved to the resolution of the GBT beam in the Ka band (i.e., 25'') following the image registration method of Aniano et al. (2011). Using the combination of all infrared data, total infrared (IR; 8 – 1000  $\mu\text{m}$ ) emission and uncertainty maps were constructed using the models of Draine & Li (2007) as described in G. Aniano (2012, submitted).

For each data set, the flux density at the position of each GBT pointing is the surface brightness multiplied by the beam solid angle. Uncertainties on the photometry are estimated as a combination of the calibration and beam-size uncertainties; we assign a 17% uncertainty to account for the dispersion in the beam areas among our sets of GBT observations as given in §3.1.

In the case of the UV and H $\alpha$  photometry, we correct each region for Milky Way extinction using Schlegel et al. (1998) assuming  $A_V/E(B - V) = 3.1$  and the modeled extinction curves of Weingartner & Draine (2001); Draine (2003). The multi-wavelength photometry is given in Tables 3 and 4, along with the corresponding 1- $\sigma$  errors, for the nuclei and extranuclear regions, respectively.

### 3.3. Star Formation Rate Calibrations

For the non-AGN sources in the sample, we can estimate star formation rates using the new GBT 33 GHz data. In this section we present the calibrations given in Murphy et al. (2011), where more details about their derivations can be found. These calibrations, which update those found in Kennicutt (1998) and have been adopted by Kennicutt & Evans (2012), were calculated using Starburst99 (Leitherer et al. 1999) for a common IMF so that each diagnostic can be compared fairly. A summary of these relations can be found in the Appendix Table 8.

We choose a Kroupa (Kroupa 2001) IMF, having a slope of  $-1.3$  for stellar masses between  $0.1 - 0.5 M_\odot$  and  $-2.3$  for stellar masses ranging between  $0.5 - 100 M_\odot$ . Assuming solar metallicity and a continuous, constant star formation rate over  $\sim 100$  Myr, Starburst99 stellar population models yield the following relation between the star formation rate and production rate of ionizing photons,  $Q(H^0)$ :

$$\left(\frac{\text{SFR}}{M_\odot \text{ yr}^{-1}}\right) = 7.29 \times 10^{-54} \left[\frac{Q(H^0)}{\text{s}^{-1}}\right]. \quad (1)$$

Since the ionizing flux comes from very massive stars with lifetimes  $\lesssim 10$  Myr, we note that the coefficient in Equation 1 is nearly independent of starburst age under the assumption of continuous star formation so long as it is  $\gtrsim 10$  Myr. Accordingly, such measurements sample the current (i.e.,  $\sim 10$  Myr) star formation activity. The integrated UV spectrum is also dominated by young stars, however, it is sensitive to a significantly longer timescale of recent ( $\sim 10 - 100$  Myr; Kennicutt 1998; Calzetti et al. 2005; Salim et al. 2007) star formation activity. We convolve the output Starburst99 spectrum with the *GALEX* FUV transmission curve to obtain the following conversion between star formation rate and FUV luminosity,

$$\left(\frac{\text{SFR}_{\text{FUV}}}{M_\odot \text{ yr}^{-1}}\right) = 4.42 \times 10^{-44} \left(\frac{L_{\text{FUV}}}{\text{erg s}^{-1}}\right). \quad (2)$$

Similarly, we can write such an expression for the *GALEX* NUV band such that,

$$\left(\frac{\text{SFR}_{\text{NUV}}}{M_\odot \text{ yr}^{-1}}\right) = 7.15 \times 10^{-44} \left(\frac{L_{\text{NUV}}}{\text{erg s}^{-1}}\right). \quad (3)$$

The ionizing photon rate can of course be expressed as a (extinction corrected) H recombination line flux, such

that for Case B recombination, and assuming an electron temperature  $T_e = 10^4$  K, the H $\alpha$  recombination line strength is related to the star formation rate by

$$\left(\frac{\text{SFR}_{\text{H}\alpha}}{M_\odot \text{ yr}^{-1}}\right) = 5.37 \times 10^{-42} \left(\frac{L_{\text{H}\alpha}}{\text{erg s}^{-1}}\right). \quad (4)$$

The above equation indicates that the star formation rate is directly proportional to the H $\alpha$  line luminosity, assuming that a constant fraction (i.e.,  $\approx 45\%$ ) of the ionized H atoms will emit an H $\alpha$  photon as they recombine, and that the extinction correction is accurate. However, if a significant fraction of ionizing photons are absorbed by dust, the above equation will underestimate the star formation rate, and the = sign should be replaced by  $\geq$ .

Similarly, at high radio frequencies, where  $\tau \ll 1$ , the ionizing photon rate is directly proportional to the thermal spectral luminosity,  $L_\nu^T$ , varying only weakly with electron temperature  $T_e$  (Rubin 1968), such that

$$\left[\frac{Q(H^0)}{\text{s}^{-1}}\right] = 6.3 \times 10^{25} \left(\frac{T_e}{10^4 \text{ K}}\right)^{-0.45} \left(\frac{\nu}{\text{GHz}}\right)^{0.1} \left(\frac{L_\nu^T}{\text{erg s}^{-1} \text{ Hz}^{-1}}\right). \quad (5)$$

By combining Equations 1 and 5, one can derive a relation between the star formation rate and thermal radio emission:

$$\left(\frac{\text{SFR}_\nu^T}{M_\odot \text{ yr}^{-1}}\right) = 4.6 \times 10^{-28} \left(\frac{T_e}{10^4 \text{ K}}\right)^{-0.45} \left(\frac{\nu}{\text{GHz}}\right)^{0.1} \left(\frac{L_\nu^T}{\text{erg s}^{-1} \text{ Hz}^{-1}}\right). \quad (6)$$

As with the H recombination line fluxes,  $Q(H^0)$ , and consequently the star formation rate, may in fact be underestimated by the free-free emission if a significant fraction of ionizing photons are absorbed by dust; in this case the = sign in the above equation should be replaced by  $\geq$ . However, it is worth noting that unlike free-free emission, which arises directly from the ionized gas, optical/NIR H recombination line fluxes may also suffer extinction internal to the HII region itself, resulting in an even larger deficit. For example, the extinction *internal* to HII regions in the starbursting dwarf galaxy NGC 5253 is measured to be quite large ( $A_V = 16 - 18$  mag; Turner et al. 2003).

At lower radio frequencies, which are typically dominated by non-thermal synchrotron emission, calibrations between the supernova rate, and thus the star formation rate, have been developed. From the output of Starburst99, which assumed a supernova cut-off mass of  $8 M_\odot$ , we find that the total core-collapse supernova rate,  $\dot{N}_{\text{SN}}$ , is related to the star formation rate by,

$$\left(\frac{\text{SFR}}{M_\odot \text{ yr}^{-1}}\right) = 86.3 \left(\frac{\dot{N}_{\text{SN}}}{\text{yr}^{-1}}\right). \quad (7)$$

Work comparing the non-thermal spectral luminosity with the supernova rate in the Galaxy has yielded an

empirical calibration such that

$$\left( \frac{L_\nu^{\text{NT}}}{\text{erg s}^{-1} \text{ Hz}^{-1}} \right) = 1.3 \times 10^{30} \left( \frac{\dot{N}_{\text{SN}}}{\text{yr}^{-1}} \right) \left( \frac{\nu}{\text{GHz}} \right)^{-\alpha^{\text{NT}}}, \quad (8)$$

where  $\alpha^{\text{NT}}$  is the non-thermal radio spectral index (Tammann 1982; Condon & Yin 1990). By combining Equations 7 and 8, we can express the star formation rate as a function of the non-thermal radio emission where

$$\left( \frac{\text{SFR}_\nu^{\text{NT}}}{M_\odot \text{ yr}^{-1}} \right) = 6.64 \times 10^{-29} \left( \frac{\nu}{\text{GHz}} \right)^{\alpha^{\text{NT}}} \left( \frac{L_\nu^{\text{NT}}}{\text{erg s}^{-1} \text{ Hz}^{-1}} \right). \quad (9)$$

Since it will take  $\sim 30$  Myr for  $8 M_\odot$  stars to go supernova, and the radiating lifetimes of CR electrons can be on the order of tens of Myr in normal galaxies, the non-thermal emission is sensitive to slightly longer timescales than free-free or H recombination line emission.

The observed radio continuum emission comprises both free-free and synchrotron emission. Therefore, we can combine Equations 6 and 9 to construct a single expression for the star formation rate from the total radio continuum emission at a given frequency such that:

$$\left( \frac{\text{SFR}_\nu}{M_\odot \text{ yr}^{-1}} \right) = 10^{-27} \left[ 2.18 \left( \frac{T_e}{10^4 \text{ K}} \right)^{0.45} \left( \frac{\nu}{\text{GHz}} \right)^{-0.1} + 15.1 \left( \frac{\nu}{\text{GHz}} \right)^{-\alpha^{\text{NT}}} \right]^{-1} \left( \frac{L_\nu}{\text{erg s}^{-1} \text{ Hz}^{-1}} \right). \quad (10)$$

This equation essentially weights the observed radio continuum luminosity based on the expected thermal fraction at a given frequency. As pointed out above, the thermal and non-thermal emission timescales are mismatched, with free-free emission being sensitive to massive stars with ages  $\lesssim 10$  Myr and the non-thermal emission being most sensitive to the lowest mass (i.e.,  $\gtrsim 8 M_\odot$ ) supernova progenitors having lifetimes of  $\lesssim 30$  Myr. However, Equation 10 should hold under the assumption of continuous star formation on timescales  $\gtrsim 30$  Myr.

In our analysis we have assumed an electron temperature of  $T_e = 10^4$  K when calculating star formation rates using Equations 6 and 10. However, variations in the actual electron temperatures will inject scatter into our observed trends. For instance, assuming a value of  $T_e$  as low as 5000 K will result in star formation rates that are 37 and 21% larger than assuming  $T_e = 10^4$  K using equations 6 and 10, respectively. Thus, we expect any scatter introduced by the assumption of a constant electron temperature to be smaller than these values.

#### 4. RESULTS

In the following section we estimate the fraction of thermal emission at 33 GHz and compare a number of star formation rate diagnostics with those derived using the GBT 33 GHz data. The assumption is made that the 33 GHz data provide the most reliable estimate as they are highly sensitive to free-free emission arising from the ionized gas in HII regions. While we adopt the calibrations given above (i.e., Murphy et al. 2011), we derive our own empirical relations and compare with others found in the literature.

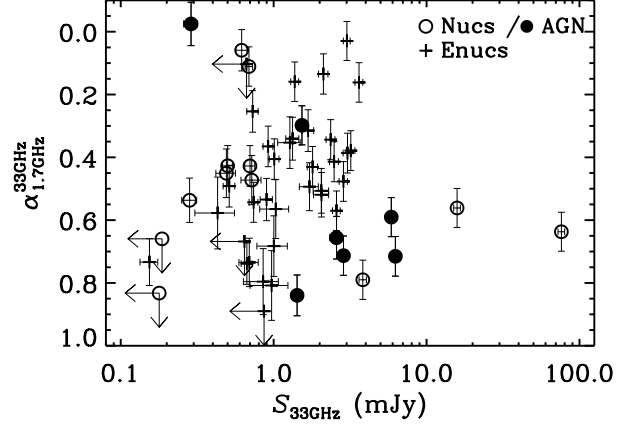


**Figure 2.** Radio spectral indices measured between 1.7 and 33 GHz plotted against 33 GHz flux densities for all 53 galaxy nuclei (circles) and extranuclear star-forming regions (crosses) having 1.7 GHz measurements. Nuclei identified as AGN in Table 1 are plotted using filled symbols. Upper limits for the 33 GHz flux densities, and corresponding spectral index measurements, are shown as arrows. Sources for which the major axis of the 1.7 GHz data was larger than the FWHM of the GBT beam at 33 GHz are not included due to imprecise matched photometry.

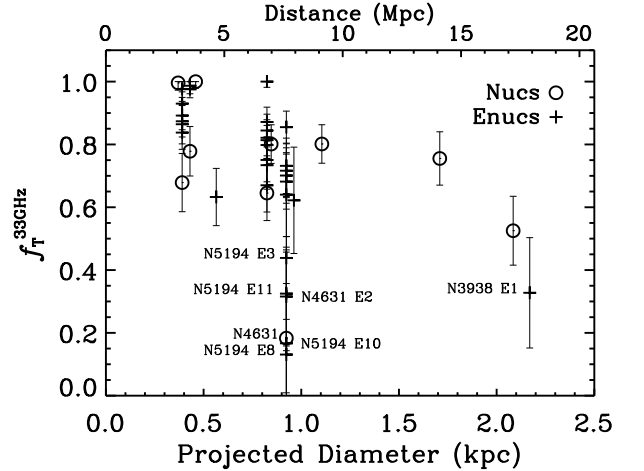


**Figure 3.** Estimates for the thermal fraction at 33 GHz plotted against the projected diameter of the GBT beam for all (i.e., 41) non-AGN sources with 33 GHz detections and corresponding 1.7 GHz data. Nuclei and extranuclear regions are shown by circles and crosses, respectively. Only a weak trend is found with distance, suggesting that the 33 GHz star formation rates are not significantly affected by averaging over larger physical areas, which should increase the amount of non-thermal emission at 33 GHz, for the more distant sources. The seven sources having 33 GHz thermal fractions  $< 50\%$  are identified, five of which required a correction for badly placed off-nod positions. These are the same seven sources having star formation rates discrepant by more than a factor of  $> 1.5$  in Figure 4 (see §4.1).

##### 4.1. Radio Spectral Indices and Estimates for the Thermal Fraction at 33 GHz

In Figure 2 the radio spectral indices measured between 1.7 and 33 GHz are shown for all 53 sources having data at 1.7 GHz with a resolution that is equal to, or higher than, the GBT data. AGN are identified among the galaxy nuclei, typically having radio spectral indices that are steeper than the rest of the sources. Using the

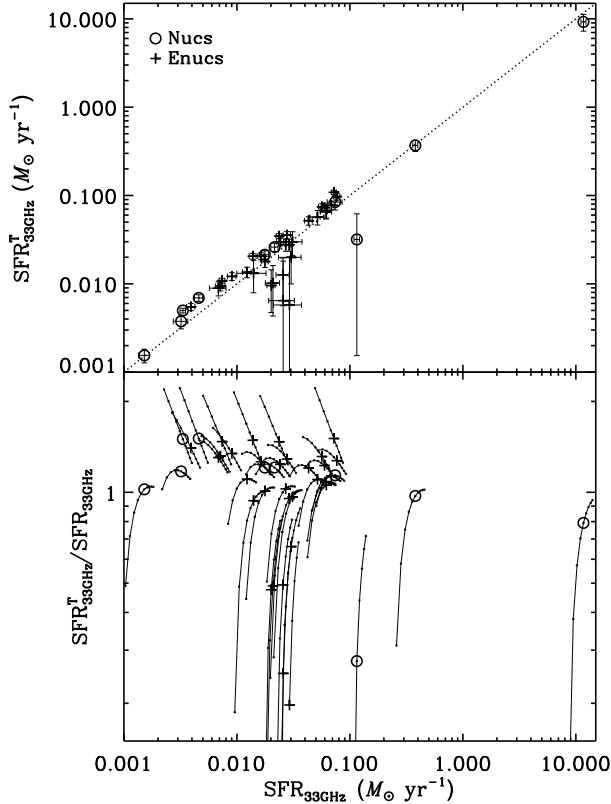


**Figure 4.** *Top:* The 33 GHz star formation rates calculated in two ways for non-AGN sources having lower frequency radio data, allowing for an estimate for the 33 GHz thermal fraction. Star formation rates calculated using the thermal emission at 33 GHz and Equation 6 are given along the ordinate while star formation rates calculated using the total 33 GHz spectral luminosity along with Equation 10, assuming a non-thermal radio spectral index of  $\alpha^{\text{NT}} = -0.85$  are given along the abscissa. Also shown is a one-to-one (dotted) line. The seven sources having star formation rates discrepant by more than a factor of  $>1.5$  are the same seven sources identified in Figure 3 (see §4.1). *Bottom:* The ratio of the two 33 GHz star formation rate estimates, illustrating the effect of assuming different values for the non-thermal radio spectral index, ranging between 0.6–1.05 (left to right) in increments of 0.05. The open circles assume  $\alpha^{\text{NT}} = -0.85$ , as in the above comparison.

spectral index information over this rather long lever-arm, we can estimate the thermal emission fraction at 33 GHz if we assume a fixed non-thermal spectral index. We assume a constant non-thermal radio spectral index of  $\alpha^{\text{NT}} = 0.85$  given that this was the average non-thermal spectral index found among the 10 star-forming regions studied in NGC 6946 by Murphy et al. (2011). Furthermore, this is very close to the value found by Niklas et al. (1997, i.e.,  $\alpha^{\text{NT}} = 0.83$  with a scatter of  $\sigma_{\alpha^{\text{NT}}} = 0.13$ ) for a sample of 74 nearby galaxies. We do not estimate the thermal fractions for galaxy nuclei containing AGN since there is likely to be more variation in their intrinsic non-thermal slope. Following Klein et al. (1984), and assuming that the free-free emission is optically thin, we estimate the thermal fraction such that

$$f_{\text{T}}^{\nu_1} = \frac{\left(\frac{\nu_2}{\nu_1}\right)^{-\alpha} - \left(\frac{\nu_2}{\nu_1}\right)^{-\alpha^{\text{NT}}}}{\left(\frac{\nu_2}{\nu_1}\right)^{-0.1} - \left(\frac{\nu_2}{\nu_1}\right)^{-\alpha^{\text{NT}}}}, \quad (11)$$

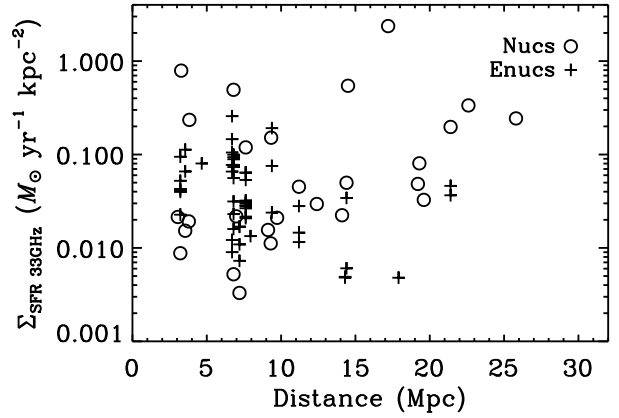


**Figure 5.** The 33 GHz star formation rates normalized by the projected area of the GBT beam (i.e., spanning  $\approx 0.15 - 11 \text{ kpc}^2$ ) plotted against distance for all (i.e., 81) non-AGN detected sources in the sample. Nuclei and extranuclear regions are shown by circles and crosses, respectively. Only a weak trend is found with distance, suggesting that the 33 GHz star formation rates are not significantly affected by averaging over larger physical areas, which should increase the amount of non-thermal emission at 33 GHz, for the more distant sources. Error bars are not shown since they are typically smaller than the plotting symbols.

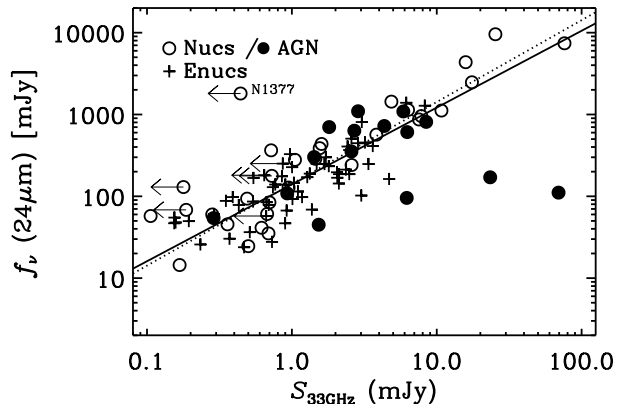


**Figure 6.** The  $24 \mu\text{m}$  flux densities plotted against corresponding (corrected) 33 GHz flux densities for the entire sample of 103 galaxy nuclei (circles) and extranuclear star-forming regions (crosses). Nuclei identified as AGN in Table 1 are indicated by filled symbols. Upper limits for the 33 GHz flux densities are shown as arrows. Error bars are not shown since they are typically smaller than the plotting symbols. Over-plotted is an ordinary least squares fit to the detected extranuclear regions and non-AGN nuclei (solid line), along with a one-to-one line scaled by the median  $24 \mu\text{m}$  to 33 GHz flux density ratio  $< f_{\nu}(24 \mu\text{m})/S_{33 \text{ GHz}} > = 142$  (dotted line). A number of AGN are clearly radio loud at 33 GHz relative to the main correlation between the  $24 \mu\text{m}$  and 33 GHz flux densities. The galaxy furthest above the fit to the main trend, which is detected at  $24 \mu\text{m}$  but not at 33 GHz, is NGC 1377. This galaxy is identified as being possibly a nascent starburst (e.g., Roussel et al. 2003, 2006).

where, for our specific case,  $\nu_1 = 33 \text{ GHz}$ ,  $\nu_2 = 1.7 \text{ GHz}$ ,  $\alpha$  is the observed radio spectral index between  $\nu_1$  and  $\nu_2$ , and we fix the thermal radio spectral index to 0.1. We find a median 33 GHz thermal fraction of  $\approx 76\%$  among all sources, with a lower and upper quartile of 64 and 87%, respectively (see Figure 3). While this method has been shown to overestimate thermal fractions for star-forming regions in a high-resolution radio study of

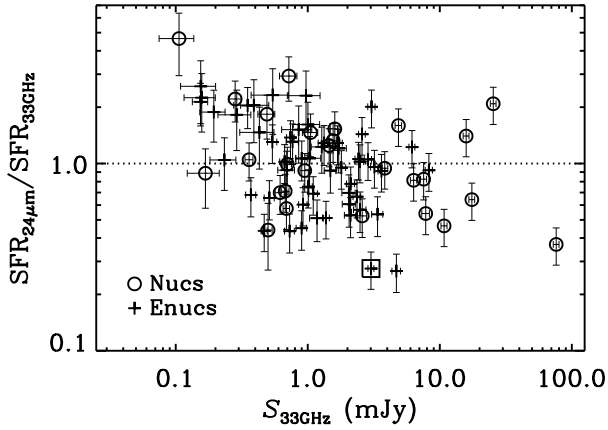


**Figure 7.** The ratio of 24  $\mu\text{m}$  to 33 GHz star formation rates plotted against the 33 GHz star formation rates for all (i.e., 81) non-AGN detected sources in the sample. Nuclei and extranuclear regions are shown by circles and crosses, respectively. The scatter about unity is  $\approx 0.25$  dex. Extranuclear region 4 in NGC 6946 is identified using a square, as the 33 GHz flux density of this source is complicated by the presence of anomalous dust emission (Murphy et al. 2010; Scaife et al. 2010).

M33 (Tabatabaei et al. 2007), those authors assumed a much steeper non-thermal index (i.e.,  $\alpha^{\text{NT}} = 1.0$ ) than adopted here. Non-thermal spectral indices have been found to be significantly flatter than 1.0 around giant HII regions based on comparisons between multifrequency radio and de-reddened H $\alpha$  observations in NGC 6946 (F. Tabatabaei et al. 2012, in preparation). Assuming  $\alpha^{\text{NT}} = 1.0$  would increase our thermal fraction estimates to  $< f_{\text{T}}^{33\text{GHz}} > \approx 85$  with a dispersion of 15%.

In Figure 4 we plot star formation rates for all non-AGN sources having low frequency radio data, allowing us to estimate the 33 GHz thermal fraction, in two ways. We first compute 33 GHz star formation rates using only the thermal fraction at 33 GHz and Equation 6. In the top panel of 4, these are plotted against 33 GHz star formation rates using the total 33 GHz spectral luminosity with Equation 10, again assuming a non-thermal spectral index of  $\alpha^{\text{NT}} = 0.85$ . There are 6 sources (i.e., NGC 3938 Enuc. 1, NGC 4631, NGC 4631 Enuc. 2, NGC 5194 Enuc. 8, NGC 5194 Enuc. 10, and NGC 5194 Enuc. 11) with star formation rate estimates that are discrepant by more than a factor of  $\sim 2$ . This discrepancy may arise from our assumption for the non-thermal spectral index being too flat; these are the only sources shown in Figure 2 for which  $\alpha_{1.7\text{GHz}}^{33\text{GHz}} > 0.70$ , and are also the only sources in Figure 3 having thermal fractions  $< 40\%$ . For the two observations towards NGC 4631, we might expect a steeper spectral index as the galaxy is observed to be edge-on, and has a very prominent non-thermal radio component. Observing through the disk of this source could lead to a significant amount of diffuse non-thermal emission in the beam, steepening the observed spectrum. However, for the remaining four sources, NGC 3938 Enuc. 1, NGC 5194 Enuc. 10, and NGC 5194 Enuc. 11, it is worth noting that the 33 GHz photometry required a correction for badly placed off-nod positions; underestimating the corrections will result in artificially steep spectral index estimates. In the top panel of Figure 4 we also plot a one-

to-one line, showing that these two estimates are generally consistent with one another. The dispersion about an ordinary least squares fit line is less than  $\approx 0.05$  dex (i.e., 12%).

In the bottom panel of Figure 4, we plot the ratio of these two star-formation rate estimates, illustrating the effect for different assumptions of  $\alpha^{\text{NT}}$ . We allow  $\alpha^{\text{NT}}$  to range between 0.6 – 1.05 (left to right) in increments of 0.05. Except for the six discrepant sources identified above, the two estimates appear generally consistent within errors when varying the assumption for the non-thermal radio spectral index. Given the extremely good agreement between these two estimates, which may not be terribly surprising given that the 33 GHz flux densities are generally dominated by thermal emission, star formation rates estimated using Equation 10 are assumed as our reference value for comparisons throughout the paper. By using Equation 10, we are able to calculate star formation rates for the entire sample (i.e., lower frequency radio data are not necessarily required). Before moving on, it is worth investigating how the variations in the physical size of the GBT beam may affect the star formation rate estimates given that Equation 10 does not take into account morphological differences between the (compact) free-free and (diffuse) non-thermal emission in galaxies.

#### 4.1.1. Distance Effects

The distances to the galaxies being investigated vary by a factor of  $\sim 10$ . Consequently, the physical areas our observations average over span a factor of  $\sim 100$ . By averaging over larger pieces of each galaxy, more diffuse emission is introduced into each beam relative to additional emission from compact HII regions and, for the 33 GHz observations, likely introduces more non-thermal emission. To investigate the consequence of this effect, we plot the 33 GHz thermal fraction estimates as a function of the projected diameter of the region being measured in Figure 3. We find large (i.e.,  $\approx 93_{-10}^{+7}\%$ ) thermal fractions for all sources having sizes  $\lesssim 0.5$  kpc, and a larger mix of thermal fractions for larger diameters. Excluding the 6 sources having thermal fractions  $\lesssim 40\%$ , as they may be artificially low (see above), there does appear to be a weak trend of decreasing thermal fraction with increasing projected area. However, it is hard to reliably quantify any trend given that there are so few sources with lower frequency radio data at the large distance end of the sample.

To look at the effect of distance in another way, we plot the 33 GHz star formation rates, normalized by the projected area of the beam, versus distance in Figure 5 for all detected, non-AGN sources. We calculate star formation rates using Equation 10, with  $\alpha^{\text{NT}} = 0.85$ , since this expression takes both thermal and non-thermal emission components into account. If the star formation rate calibration is being affected by the inclusion of a substantial amount of non-thermal emission for the more distant galaxies, we would expect a trend of increasing star formation rate per unit area as the beam size increases. Perhaps there is a weak trend; the median star formation rate surface density at distances below and above 15 Mpc is  $\approx 0.03$  and  $\approx 0.08 M_{\odot} \text{ yr}^{-1} \text{ kpc}^2$ , respectively. However, the lack of a meaningful number of sources, es-

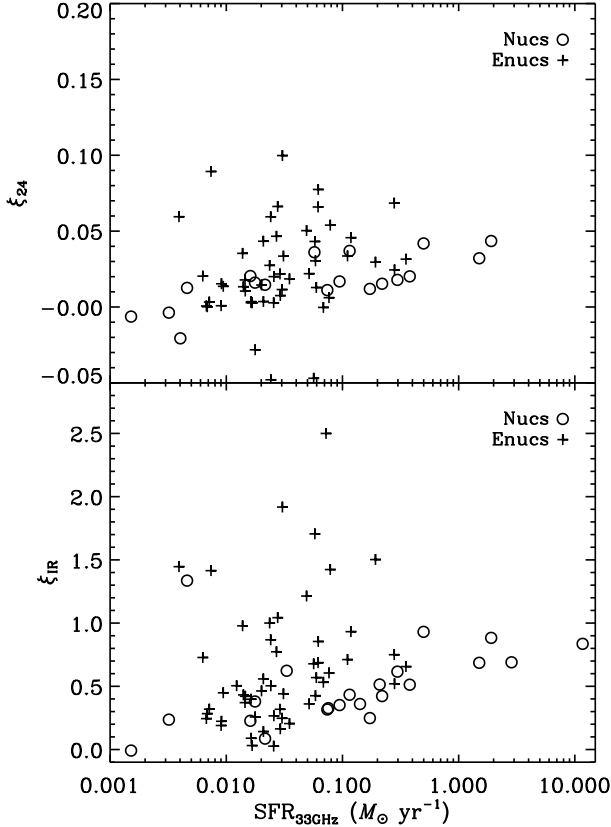


**Figure 8.** *Top:* The  $24\ \mu\text{m}$  scaling factor for computing  $\text{H}\alpha + 24\ \mu\text{m}$  star formation rates plotted against the 33 GHz star formation rates for all non-AGN detected regions. *Bottom:* The IR scaling factor for computing FUV+IR star formation rates plotted against the 33 GHz star formation rates for all non-AGN detected regions.

pecially extranuclear regions, at  $d > 15\ \text{Mpc}$ , makes it difficult to quantify any trend. Thus, it appears that larger beams do not significantly affect our 33 GHz star formation rate estimates.

#### 4.2. Comparison with $24\ \mu\text{m}$ Warm Dust Emission

Unlike the far-infrared continuum emission, for which a non-negligible fraction may be powered by an older stellar population (e.g., Sauvage & Thuan 1992; Walterbos & Greenawalt 1996; Bendo et al. 2010), warm dust emission appears to be more tightly correlated to the current star formation activity in the disks of galaxies (e.g., Helou et al. 2004; Murphy et al. 2006a). Consequently, a number of calibrations relating the warm dust emission at  $24\ \mu\text{m}$  to star formation rates have been introduced in the literature (e.g., Wu et al. 2005; Pérez-González et al. 2006; Alonso-Herrero et al. 2006; Calzetti et al. 2007; Relaño et al. 2007; Zhu et al. 2008; Rieke et al. 2009); a detailed comparison among each of these relations can be found in Calzetti et al. (2010).

In Figure 6 we plot  $24\ \mu\text{m}$  flux densities against corresponding (corrected) 33 GHz flux densities for the entire sample of 103 galaxy nuclei and extranuclear regions. Apart from the galaxy nuclei that are known to harbor AGN, a number of which are radio loud at 33 GHz relative to the observed  $24\ \mu\text{m}$  emission, there is a fairly tight correlation between the  $24\ \mu\text{m}$  and 33 GHz flux densities. The only other clearly outlying source is NGC 1377,

which has a large  $24\ \mu\text{m}$  flux and remains undetected at 33 GHz. This galaxy is thought to be experiencing a nascent starburst, for which it is within a few Myr of the onset of an intense star formation episode after being quiescent for at least  $\sim 100\ \text{Myr}$  (e.g., Roussel et al. 2003, 2006). This starburst, while heating the dust, has yet to produce detectable free-free emission, nor observable signatures of CRs. Over-plotted in Figure 6 are both a one-to-one line, scaled by the median  $24\ \mu\text{m}$  to 33 GHz flux density ratio  $\langle f_\nu(24\ \mu\text{m})/S_{33\ \text{GHz}} \rangle = 142$ , and an ordinary least squares fit to all non-AGN sources detected at 33 GHz given by,

$$\left[ \frac{f_\nu(24\ \mu\text{m})}{\text{mJy}} \right] = 140 \left( \frac{S_{33\ \text{GHz}}}{\text{mJy}} \right)^{0.94}, \quad (12)$$

which are consistent within errors. The scatter about the ordinary least squares fit is  $\sim 0.26$  dex.

After converting the  $24\ \mu\text{m}$  flux densities into luminosities, we relate these to corresponding 33 GHz star formation rate estimates to come up with the following relation among all non-AGN detected sources,

$$\left( \frac{\text{SFR}_{24\ \mu\text{m}}}{M_\odot\ \text{yr}^{-1}} \right) = 3.1 \times 10^{-38} \left[ \frac{\nu L_\nu(24\ \mu\text{m})}{\text{erg s}^{-1}} \right]^{0.88}. \quad (13)$$

The fitting coefficients are consistent with others in the literature (for a detailed compilation see Calzetti et al. 2010). In Figure 7 we plot the ratio of the  $24\ \mu\text{m}$  to 33 GHz star formation rate against the 33 GHz star formation rates finding that the scatter about this relation is  $\approx 0.25$  dex. The square identifies the location of the anomalous dust detection in NGC 6946 (Murphy et al. 2010; Scaife et al. 2010), which may also explain why other sources lie significantly below the unity line.

We might expect different relations between warm  $24\ \mu\text{m}$  dust emission per unit star formation rate among the extranuclear regions and nuclei due to additional old stellar population heating of grains by galaxy bulges. To investigate this, we can separate our sample, and measure the median ratio of the  $24\ \mu\text{m}$  spectral luminosity to 33 GHz star formation rate for the nuclei and extranuclear regions. The average ratios, along with the associated dispersions, are given in Table 5. Within the scatter, which is just under a factor of  $\sim 2$ , the median ratios are consistent with one another, as well as with the median ratio for all non-AGN detected sources. Comparing the ratio of the total IR luminosity to 33 GHz star formation rate for nuclei, extranuclear regions, and all non-AGN detected sources, we again find that the median values are consistent. Accordingly, we can use these average ratios to write empirical relations between the  $24\ \mu\text{m}$  spectral luminosity and total IR luminosity with the star formation rate that should be reliable to within a factor of  $\sim 2$  such that,

$$\left( \frac{\text{SFR}_{24\ \mu\text{m}}^{\text{Avg.}}}{M_\odot\ \text{yr}^{-1}} \right) = 2.45 \times 10^{-43} \left[ \frac{\nu L_\nu(24\ \mu\text{m})}{\text{erg s}^{-1}} \right], \quad (14)$$

and

$$\left( \frac{\text{SFR}_{\text{IR}}^{\text{Avg.}}}{M_\odot\ \text{yr}^{-1}} \right) = 3.15 \times 10^{-44} \left( \frac{L_{\text{IR}}}{\text{erg s}^{-1}} \right). \quad (15)$$

We note that the the coefficient equating the to-

tal IR luminosity with star formation rate derived in Murphy et al. (2011) is  $\approx 23\%$  larger than this empirically measured coefficient, and thus consistent given the nearly factor of  $\sim 2$  scatter.

#### 4.3. Comparison with $H\alpha$ and $24\ \mu\text{m}$ Emission

Given that not all of the UV/optical photons will be absorbed and re-radiated by dust, a series of new empirical calibrations based on the linear combination of observed  $24\ \mu\text{m}$  (obscured star formation) and  $H\alpha$  (unobscured star formation) luminosities have been developed (e.g., Calzetti et al. 2007; Kennicutt et al. 2007, 2009; Zhu et al. 2008). These empirical star formation recipes usually take the form of

$$\left(\frac{\text{SFR}_{\text{mix}}}{M_{\odot}\ \text{yr}^{-1}}\right) = 5.37 \times 10^{-42} \left[\frac{L_{H\alpha} + \xi_{24}\nu L_{\nu}(24\ \mu\text{m})}{\text{erg s}^{-1}}\right], \quad (16)$$

where the coefficient  $\xi_{24}$ , scaling the warm  $24\ \mu\text{m}$  dust emission, has been found to vary depending on the physical scale being investigated. For instance, on the scale of individual HII regions,  $\xi_{24} \approx 0.031$  (Calzetti et al. 2007), where as for whole galaxies  $\xi_{24} \approx 0.020$  (Kennicutt et al. 2009). A luminosity dependence has also been found, with  $\xi_{24}$  increasing with the  $24\ \mu\text{m}$  luminosity of a galaxy (Calzetti et al. 2010).

Combining the 33 GHz star formation rates with the available  $H\alpha$  and  $24\ \mu\text{m}$  photometry, we can estimate  $\xi_{24}$  for the star-forming (i.e., non-AGN) regions in our sample. These values are plotted in the top panel of Figure 8 against the 33 GHz star formation rates, showing a large scatter. The median and dispersion are  $\xi_{24} = 0.018 \pm 0.004$  and  $\sigma_{\xi_{24}} = 0.031$ , respectively. Thus, on  $\sim\text{kpc}$  scales, which likely average over many non-coeval HII regions, the scaling coefficient appears to be similar to that for entire galaxies. It is also worth noting that the scatter is quite large, which most likely arises from both the large range in physical sizes being covered by the GBT beam among the entire sample, as well as the difficulty in matching the GBT and imaging photometry.

#### 4.4. Comparison with Total IR and UV Emission

Similarly, by combining the star formation rate estimates from the total IR and (observed) UV emission, one can account for the obscured and unobscured emission contributing to the total (bolometric) star formation rate, which we define as:

$$\text{SFR}_{\text{tot}} = \text{SFR}_{\text{FUV}} + \text{SFR}_{\text{IR}}. \quad (17)$$

This diagnostic is often used to characterize star formation rates from galaxies in both low- (e.g., Iglesias-Páramo et al. 2006; Buat et al. 2007, 2011) and high- $z$  (e.g., Iglesias-Páramo et al. 2004; Elbaz et al. 2007; Daddi et al. 2007; Reddy et al. 2010) studies.

Using the above calibration for the FUV star formation rate (i.e., Equation 2), this relation can be expressed as a linear combination of the UV and total IR emission such that,

$$\left(\frac{\text{SFR}_{\text{tot}}}{M_{\odot}\ \text{yr}^{-1}}\right) = 4.42 \times 10^{-44} \left(\frac{L_{\text{FUV}} + \xi_{\text{IR}}L_{\text{IR}}}{\text{erg s}^{-1}}\right), \quad (18)$$

where the coefficient  $\xi_{\text{IR}}$ , scaling the total IR emission, has been found to be  $\sim 0.46$  for normal star-forming galaxies (Hao et al. 2011) and as large as  $\sim 0.6$  for starburst

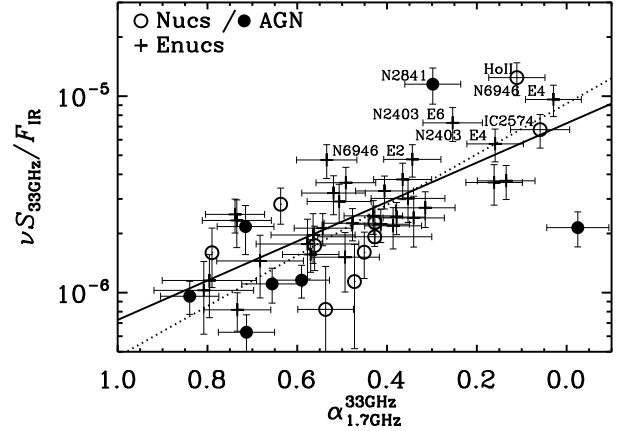


**Figure 9.** The ratio of the 33 GHz to total infrared (IR;  $8 - 1000\ \mu\text{m}$ ) fluxes plotted as a function of radio spectral index measured between 1.7 and 33 GHz. Nuclei and extranuclear regions are shown by circles and crosses, respectively, and AGN are identified by filled circles. The solid line is the ordinary least squares fit to the data, while the dotted line illustrates the expected trend for a fixed ratio of  $\nu S_{1.7\ \text{GHz}}/F_{\text{IR}}$ . We show the names for sources having both flux ratios  $\nu S_{33\ \text{GHz}}/F_{\text{IR}} > 4 \times 10^{-6}$  and spectral indices  $\alpha_{1.7\ \text{GHz}}^{33\ \text{GHz}} < 0.5$  as these sources lie near the position of NGC 6946 Enuc. 4 (Murphy et al. 2010; Scaife et al. 2010) in this plot, and may be good candidates for containing anomalous dust emission.

galaxies (e.g., Meurer et al. 1999; Calzetti 2001). These empirical values are significantly smaller than the value of 0.88 reported in Murphy et al. (2011), which assumed that the entire Balmer continuum was absorbed and re-radiated in the infrared for their derived IR star formation rate calibration of individual star-forming complexes.

Using our 33 GHz star formation rates, we estimate  $\xi_{\text{IR}}$  for the star-forming regions in our sample and plot them in the bottom panel of Figure 8 against the 33 GHz star formation rates. The median and dispersion are  $\xi_{\text{IR}} = 0.50 \pm 0.05$  and  $\sigma_{\xi_{\text{IR}}} = 0.47$ , respectively. The scatter is even larger than that for  $\xi_{24}$ , which may arise from the fact that a calibration such as this depends on the range of ages among individual star formation sites in each star-forming complex covered by the GBT 33 GHz beam. Thus, we expect increasing uncertainties in such a calibration when applied to a single star-forming region depending on how well the IR and UV are measuring emission from recent star formation, not to mention the fact that the IR and UV are sensitive to star formation on different timescales (i.e.,  $\sim 10\ \text{Myr}$  versus  $\sim 10 - 100\ \text{Myr}$ , respectively).

## 5. DISCUSSION

We have used new GBT 33 GHz radio continuum data to measure free-free emission toward 103 nearby galaxy nuclei and extranuclear star-forming regions. We find that the 33 GHz emission is typically dominated by free-free emission, making it a sensitive measure of the current star formation rate. Here we discuss the results of the comparisons between the 33 GHz star formation rates and other dust-sensitive estimators. We additionally discuss some instances where the 33 GHz emission may contain a contribution from anomalous dust emission and how having high frequency radio data can help infer physical properties of the star-forming complexes.

**Table 5**  
Average Infrared to 33 GHz Star Formation Rate Ratios

Sources	$\langle \log[\text{SFR}_{33\text{ GHz}}/\nu L_{\nu}(24\ \mu\text{m})] \rangle$ (dex)	$\sigma$ (dex)	$\langle \log(\text{SFR}_{33\text{ GHz}}/L_{\text{IR}}) \rangle$ (dex)	$\sigma$ (dex)
Nuc.	-42.61	0.27	-43.55	0.28
Enuc.	-42.61	0.26	-43.49	0.29
All	-42.61	0.26	-43.50	0.29

**Note.** — Median ratios are given. Only non-AGN detected sources included.

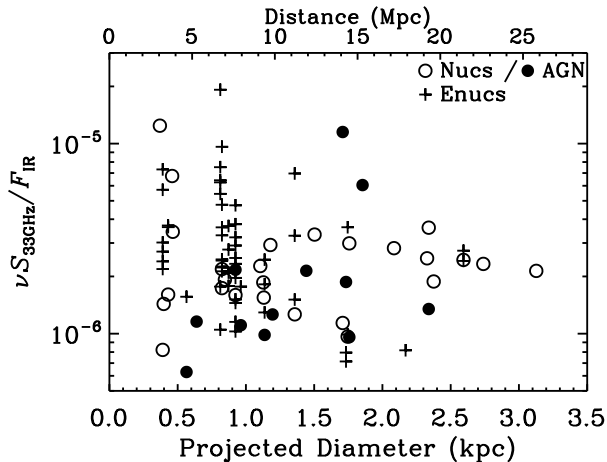


**Figure 10.** The ratio of the 33 GHz to total IR fluxes plotted as a function of projected area of the GBT 33 GHz beam. Nuclei and extranuclear regions are shown by circles and crosses, respectively, and AGN are identified by filled circles. There does not appear to be a strong trend between the flux ratio and increasing projected area.

### 5.1. Dust-Dependent Star Formation Rates

Using the 33 GHz star formation rates as a reference, we have investigated a number of dust-sensitive star formation rate indicators used in the literature. In §4.2 we find a relation between the 33 GHz star formation rates and  $24\ \mu\text{m}$  luminosity that is consistent with others in the literature. However, while similar, we do find significantly larger scatter. We believe that the increased scatter most likely arises due to a combination of several effects. First, properly matching the single-beam GBT photometry to that from the ancillary images of resolved sources is difficult, and the associated uncertainties will increase the dispersion of any trends. Additionally, the area covered by GBT beam covers a range of physical sizes in the sample, which will also inject scatter into any observed correlations. And, of course, the corrections applied in cases of potential over subtraction of sky due to reference nodes landing on bright regions of the targeted galaxy add another source of scatter.

In looking at the relation between the 33 GHz star formation rates and  $24\ \mu\text{m}$  spectral luminosities for galaxy nuclei and extranuclear regions independently, we find them to be consistent. This is also true for the relation between 33 GHz star formation rates and total IR luminosities. Thus, on average, there does not appear to be excess infrared emission per unit star formation for galaxy nuclei relative to the extranuclear star-forming complexes on the physical scales being investigated.

In §4.3 and 4.4, we investigate two hybrid star formation diagnostics that attempt to account for the un-

obsured and obscured star formation components (i.e.,  $H\alpha + 24\ \mu\text{m}$  and UV+IR). While we find scaling coefficients for the  $24\ \mu\text{m}$  and total IR luminosities that are similar to those reported in the literature, albeit with a large scatter most likely due to the reasons mentioned above, it is worth noting that the values reported are similar to those found from measurements of *entire* galaxies (e.g., Kennicutt et al. 2009; Hao et al. 2011). This agreement most likely arises because of the large area covered by the GBT beam at the distances of the sample galaxies, being roughly  $\sim 1\text{ kpc}$ , on average. Thus, on these physical scales, and by not including a local background subtraction, it appears that the star formation diagnostics presented here are applicable for globally integrated measurements of galaxies.

We summarize the final relations for each of these four dust-dependent star formation rate estimates, along with all theoretically motivated calibrations discussed in §3.3, in Appendix Table 8.

### 5.2. Variations on the Thermal Fraction and Non-Thermal Spectral Index

In Figure 9 we plot the ratio of the 33 GHz to total IR fluxes as a function of the radio spectral index measured between 1.7 and 33 GHz. There is a clear trend of increasing flux ratio with flatter spectral index. This trend does not seem to arise due to differences in the projected physical area of the 33 GHz beam among the sources (see Figure 10). In fact, this trend is opposite the expectation for distance effects: as the physical area subtended by the GBT beam increases, one would expect a larger contribution of diffuse non-thermal emission from a galaxy disk relative to additional free-free emission, thus resulting in a steeper spectral index and an increase in 33 GHz to IR flux ratios.

The ordinary least squares fit to the non-AGN sources (solid line) appears generally consistent with, albeit slightly flatter than, the expected trend assuming a fixed ratio of  $\nu S_{1.7\text{ GHz}}/F_{\text{IR}}$ ; the dotted line is given by scaling the median ratio  $\nu S_{1.7\text{ GHz}}/F_{\text{IR}}$  by  $(33/1.7)^{1-\alpha}$ . By only having radio data at two well-spaced frequencies, it is not possible to distinguish whether the spectral flattening is being driven by an increase in the thermal fraction or flattening of the non-thermal radio spectral indices. If we are to assume that this trend is in fact dominated by an increase in the thermal fraction, we can use the scatter about the ordinary least squares fit to the data to set the *maximum* dispersion for the non-thermal spectral indices among the non-AGN sources, which is found to be  $\sigma_{\alpha_{\text{NT}}} \lesssim 0.13$ . Interestingly, this is similar to the dispersion in global non-thermal spectral indices measured by Niklas et al. (1997,  $\sigma_{\alpha_{\text{NT}}} = 0.13$ ).

Again, assuming that the trend is in fact driven by a

change in thermal fraction among the sample, suggests that the non-thermal emission component may be quite similar among each star-forming region, with a nearly uniform CR electron injection spectrum and similar spectral steepening from associated energy losses (e.g., synchrotron, inverse Compton, bremsstrahlung, and ionization processes). More specifically, there must only be moderate variability in the ratio of synchrotron to total CR electron cooling processes among each of the star-forming complexes being investigated.

### 5.3. Anomalous Dust Candidates

Cosmic Microwave Background experiments were the first to discover the presence of an “anomalous” dust-correlated emission component at frequencies between  $\sim 10 - 90$  GHz (e.g., Leitch et al. 1997). In the original GBT pilot study of NGC 6946, Murphy et al. (2010) identified an extranuclear star-forming complex that had a significant amount of excess emission at 33 GHz relative to what was expected by extrapolating from multifrequency measurements at lower frequencies (i.e.,  $< 10$  GHz). While anomalous dust emission has been observed in excess of synchrotron and free-free components in Galactic HII regions (e.g., Dickinson et al. 2009), this observation of excess 33 GHz emission towards a star-forming complex in NGC 6946 is identified as the first detection of anomalous dust emission outside of the Milky Way. Now, using the full sample data, we can look for other potential extragalactic anomalous dust emitting candidates.

As stated above, Figure 9 shows a clear trend in which the ratio of 33 GHz to total IR fluxes increases as the radio spectral index measured between 1.7 and 33 GHz flattens. In Figure 9 we also show the location of NGC 6946 E nuc. 4, identified as containing anomalous dust emission (Murphy et al. 2010; Scaife et al. 2010) that accounts for  $\approx 50\%$  of the observed 33 GHz flux density. However, this source does not appear to be significantly discrepant from the expected trend in this plot. It therefore appears that identifying anomalous dust candidates with such coarse radio spectral resolution may not be possible, and a much finer sampling (i.e., better than a factor of 2 in frequency steps) is necessary.

Besides NGC 6946 E nuc. 4, there are a number of other sources that both show flat radio spectral indices with large 33 GHz to infrared flux ratios; sources having flux ratios  $\nu S_{33 \text{ GHz}}/F_{\text{IR}} > 4 \times 10^{-6}$  and observed radio spectral indices  $\alpha_{1.7 \text{ GHz}}^{33 \text{ GHz}} < 0.5$  have been highlighted as potential anomalous dust candidates in Figure 9. However, a detailed investigation of these regions to confirm or deny the presence of anomalous dust emission is outside the scope of this paper, and really requires additional radio data at finely spaced frequencies much closer to 33 GHz (e.g., between  $\sim 15$  and 90 GHz) to confirm a peaked spectrum.

### 5.4. The Nascent Starburst NGC 1377

The archetypal nascent starburst NGC 1377, which is thought to be within a few Myr of the onset of an intense star formation episode after being quiescent for at least  $\sim 100$  Myr, remains undetected in the radio even at the depth of our 33 GHz observations. Given its measured flux density at  $24 \mu\text{m}$  and the  $3\sigma$  upper limit of

0.44 mJy at 33 GHz, we would have expected a  $\sim 70\sigma$  detection. As has already been shown by Roussel et al. (2003), this non-detection in the radio most likely does not arise from the source being optically thick. Using the 33 GHz upper limit, we can set even more stringent constraints on this. Assuming an electron temperature of  $\sim 10^4$  K and  $\tau_{33 \text{ GHz}} \sim 1$  sets the expected brightness temperature and emission measure of the source to be  $\sim 6000$  K and  $\sim 5 \times 10^9 \text{ pc cm}^{-6}$ , respectively. The corresponding size of the source would therefore have to be  $< 1$  pc with an electron density of  $> 7 \times 10^5 \text{ cm}^{-3}$ . These values are significantly more extreme than the size and electron density limits of  $< 28$  pc and  $> 2700 \text{ cm}^{-3}$  inferred by Roussel et al. (2003).

Given the apparent absence of AGN activity in NGC 1377, any free-free emission associated with ongoing star formation powering the bright dust continuum appears significantly suppressed. If the nascent starburst scenario suggested by Roussel et al. (2003) is true, the lack of free-free emission detected at 33 GHz could very well arise from having extremely young, deeply embedding star formation in which the dust is absorbing  $\gtrsim 95\%$  of the ionizing photons. The absorption of such a high fraction of ionizing photons by dust would then lead to star formation rates that are overestimated by a factor of  $\sim 2$  by using calibrations relying on dust emission.

## 6. CONCLUSIONS

In the paper we have presented GBT 33 GHz photometry for 103 galaxy nuclei and extranuclear star-forming regions included as part of the Star Formation in Radio Survey. The sample galaxies are included in the *Spitzer*-SINGS and *Herschel*-KINGFISH legacy programs, and therefore have large amounts of ancillary data for future followup, including mid- and far-infrared spectral mappings. Here we summarize our main conclusions from this initial investigation.

1. Among the non-AGN sources having lower frequency radio data, we find a median thermal fraction at 33 GHz of  $\approx 76\%$  with a dispersion of  $\approx 24\%$ . For all sources resolved on scales  $\lesssim 0.5$  kpc, the thermal fraction is even larger, being  $\gtrsim 90\%$ , on average, however, there is very little lower frequency radio data for galaxies at the large distance end of the sample. This suggests that the rest-frame 33 GHz emission provides a sensitive measure of the ionizing photon rate from young star-forming regions, thus making it a robust star formation rate indicator, especially at high spatial resolution.
2. We find an increase in the 33 GHz to total IR flux ratios as the radio spectral index flattens, which does not appear to correlate with the projected area of the GBT beam, but is instead consistent with the expectation from an increase in the thermal fraction among the sources. Consequently, the ratio of non-thermal to total IR emission appears relatively constant among star-forming regions, suggesting only moderate variability in the CR electron injection spectrum and ratio of synchrotron to total cooling processes. Given the scatter in this trend, the maximum dispersion in the non-thermal radio spectral indices among these non-AGN sources is  $\sigma_{\alpha_{\text{NT}}} \lesssim 0.13$ .

3. Using the 33 GHz star formation rates as a reference, we derive scaling coefficients for the following recipes that attempt to sum the obscured and unobscured star formation components:  $H\alpha + 24 \mu\text{m}$  and UV+IR. Although we have targeted galaxy nuclei and extranuclear star-forming complexes, with a median resolution of  $\sim 1$  kpc, the hybrid scaling coefficients are consistent with those in the literature derived for globally integrated measurements of galaxies.
4. Identifying anomalous dust candidates based on a coarse sampling of the radio spectrum, even with a large lever-arm spanning 1.7, and 33 GHz, is inconclusive. A much finer (i.e., better than a factor of 2) sampling in frequency space, spanning  $\sim 15$  to 90 GHz to actually measure the peak, appears necessary for conclusive detections.
5. Given the depth of our 33 GHz photometry, we are able to put greater doubt on the possibility that NGC 1377 is radio faint due to being optically-thick at radio frequencies; the source size would need to be  $< 1$  pc with an electron density of  $> 7 \times 10^5 \text{ cm}^{-3}$ . Assuming that the source is at the onset of a starburst, the lack of detectable free-free emission at 33 GHz would require dust to absorb  $\gtrsim 95\%$  of the ionizing photons, leading infrared-derived star formation rates to be overestimated by as much as a factor of 2.

We are currently in the process of collecting  $1/4$ -sized 33 GHz maps using the VLA in the D-configuration for each of the sources targeted with the GBT, along with a few others at lower declination. These maps will have an angular resolution of  $\sim 2''$ , allowing us to sample physical scales ranging between 30 – 300 pc given the distances of the galaxy sample. At this resolution, we will be able to probe the scales of individual giant HII regions, where we expect even larger thermal fractions for more accurate estimates of star formation rates. These maps will additionally enable us to isolate the location of potential extragalactic anomalous dust emitting sources with significantly greater accuracy. An initial round of data has been taken between October 2011 and January 2012.

We thank the anonymous referee for useful suggestions that helped improve the presentation of the paper. E.J.M. thanks C. Leitherer and M. Seibert for useful discussions. The National Radio Astronomy Observatory is a facility of the National Science Foundation operated under cooperative agreement by Associated Universities, Inc. This work is based in part on observations made with the *Spitzer* Space Telescope, which is operated by the Jet Propulsion Laboratory, California Institute of Technology under a contract with NASA. *Herschel* is an ESA space observatory with science instruments provided by European-led Principal Investigator consortia and with important participation from NASA.

#### REFERENCES

- Alonso-Herrero, A., Rieke, G. H., Rieke, M. J., et al. 2006, *ApJ*, 650, 835
- Aniano, G., Draine, B. T., Gordon, K. D., & Sandstrom, K. 2011, *PASP*, 123, 1218
- Bendo, G. J., Wilson, C. D., Pohlen, M., et al. 2010, *A&A*, 518, L65+
- Bendo, G. J., Boselli, A., Dariush, A., et al. 2011, ArXiv e-prints
- Braun, R., Oosterloo, T. A., Morganti, R., Klein, U., & Beck, R. 2007, *A&A*, 461, 455
- Buat, V., Giovannoli, E., Takeuchi, T. T., et al. 2011, *A&A*, 529, A22+
- Buat, V., Takeuchi, T. T., Iglesias-Páramo, J., et al. 2007, *ApJS*, 173, 404
- Calzetti, D. 2001, *PASP*, 113, 1449
- Calzetti, D., Kennicutt, Jr., R. C., Bianchi, L., et al. 2005, *ApJ*, 633, 871
- Calzetti, D., Kennicutt, R. C., Engelbracht, C. W., et al. 2007, *ApJ*, 666, 870
- Calzetti, D., Wu, S., Hong, S., et al. 2010, *ApJ*, 714, 1256
- Ciardullo, R., Feldmeier, J. J., Jacoby, G. H., et al. 2002, *ApJ*, 577, 31
- Condon, J. J. 1992, *ARA&A*, 30, 575
- Condon, J. J., & Yin, Q. F. 1990, *ApJ*, 357, 97
- Daddi, E., Dickinson, M., Morrison, G., et al. 2007, *ApJ*, 670, 156
- Dale, D. A., Gil de Paz, A., Gordon, K. D., et al. 2007, *ApJ*, 655, 863
- Dale, D. A., Cohen, S. A., Johnson, L. C., et al. 2009, *ApJ*, 703, 517
- Dickinson, C., Davies, R. D., Allison, J. R., et al. 2009, *ApJ*, 690, 1585
- Draine, B. T. 2003, *ARA&A*, 41, 241
- Draine, B. T., & Lazarian, A. 1998a, *ApJ*, 494, L19+
- . 1998b, *ApJ*, 508, 157
- . 1999, *ApJ*, 512, 740
- Draine, B. T., & Li, A. 2007, *ApJ*, 657, 810
- Elbaz, D., Daddi, E., Le Borgne, D., et al. 2007, *A&A*, 468, 33
- Engelbracht, C. W., Rieke, G. H., Gordon, K. D., et al. 2008, *ApJ*, 678, 804
- Erickson, W. C. 1957, *ApJ*, 126, 480
- Freedman, W. L., Madore, B. F., Gibson, B. K., et al. 2001, *ApJ*, 553, 47
- Griffin, M. J., Abergel, A., Abreu, A., et al. 2010, *A&A*, 518, L3
- Hao, C.-N., Kennicutt, R. C., Johnson, B. D., et al. 2011, *ApJ*, 741, 124
- Helou, G., Roussel, H., Appleton, P., et al. 2004, *ApJS*, 154, 253
- Ho, L. C., Filippenko, A. V., & Sargent, W. L. W. 1997, *ApJS*, 112, 315
- Iglesias-Páramo, J., Buat, V., Donas, J., Boselli, A., & Milliard, B. 2004, *A&A*, 419, 109
- Iglesias-Páramo, J., Buat, V., Takeuchi, T. T., et al. 2006, *ApJS*, 164, 38
- Jewell, P. R., & Prestage, R. M. 2004, in *Society of Photo-Optical Instrumentation Engineers (SPIE) Conference Series*, Vol. 5489, Society of Photo-Optical Instrumentation Engineers (SPIE) Conference Series, ed. J. M. Oschmann Jr., 312–323
- Kennicutt, R. C., Hao, C., Calzetti, D., et al. 2009, *ApJ*, 703, 1672
- Kennicutt, R. C., Calzetti, D., Aniano, G., et al. 2011, ArXiv e-prints
- Kennicutt, Jr., R. C. 1998, *ARA&A*, 36, 189
- Kennicutt, Jr., R. C., & Evans, II, N. J. 2012, ArXiv e-prints
- Kennicutt, Jr., R. C., Armus, L., Bendo, G., et al. 2003, *PASP*, 115, 928
- Kennicutt, Jr., R. C., Calzetti, D., Walter, F., et al. 2007, *ApJ*, 671, 333
- Klein, U., & Graeve, R. 1986, *A&A*, 161, 155
- Klein, U., Wielebinski, R., & Beck, R. 1984, *A&A*, 135, 213
- Klein, U., Wielebinski, R., & Morsi, H. W. 1988, *A&A*, 190, 41
- Kobulnicky, H. A., & Johnson, K. E. 1999, *ApJ*, 527, 154
- Koyama, K., Petre, R., Gotthelf, E. V., et al. 1995, *Nature*, 378, 255
- Kroupa, P. 2001, *MNRAS*, 322, 231
- Leitch, E. M., Readhead, A. C. S., Pearson, T. J., & Myers, S. T. 1997, *ApJ*, 486, L23
- Leitherer, C., Schaerer, D., Goldader, J. D., et al. 1999, *ApJS*, 123, 3
- Leroy, A. K., Bigiel, F., de Blok, W. J. G., et al. 2012, ArXiv e-prints

- Mason, B. S., Weintraub, L., Sievers, J., et al. 2009, *ApJ*, 704, 1433
- Meurer, G. R., Heckman, T. M., & Calzetti, D. 1999, *ApJ*, 521, 64
- Mezger, P. G., & Henderson, A. P. 1967, *ApJ*, 147, 471
- Moustakas, J., Kennicutt, Jr., R. C., Tremonti, C. A., et al. 2010, *ApJS*, 190, 233
- Murphy, E. J. 2009, *ApJ*, 706, 482
- Murphy, E. J., Braun, R., Helou, G., et al. 2006a, *ApJ*, 638, 157
- Murphy, E. J., Helou, G., Braun, R., et al. 2006b, *ApJ*, 651, L111
- Murphy, E. J., Helou, G., Condon, J. J., et al. 2010, *ApJ*, 709, L108
- Murphy, E. J., Condon, J. J., Schinnerer, E., et al. 2011, *ApJ*, 737, 67
- Niklas, S., Klein, U., & Wielebinski, R. 1997, *A&A*, 322, 19
- Pérez-González, P. G., Kennicutt, Jr., R. C., Gordon, K. D., et al. 2006, *ApJ*, 648, 987
- Planck Collaboration Ade, P. A. R., Aghanim, N., et al. 2011, *A&A*, in press (arXiv:1101.2031)
- Poglitsch, A., Waelkens, C., Geis, N., et al. 2010, *A&A*, 518, L2+
- Readhead, A. C. S., Lawrence, C. R., Myers, S. T., et al. 1989, *ApJ*, 346, 566
- Reddy, N. A., Erb, D. K., Pettini, M., Steidel, C. C., & Shapley, A. E. 2010, *ApJ*, 712, 1070
- Relaño, M., Lisenfeld, U., Pérez-González, P. G., Vílchez, J. M., & Battaner, E. 2007, *ApJ*, 667, L141
- Rieke, G. H., Alonso-Herrero, A., Weiner, B. J., et al. 2009, *ApJ*, 692, 556
- Roussel, H. 2012, ArXiv e-prints
- Roussel, H., Helou, G., Beck, R., et al. 2003, *ApJ*, 593, 733
- Roussel, H., Helou, G., Smith, J. D., et al. 2006, *ApJ*, 646, 841
- Rubin, R. H. 1968, *ApJ*, 154, 391
- Salim, S., Rich, R. M., Charlot, S., et al. 2007, *ApJS*, 173, 267
- Sauvage, M., & Thuan, T. X. 1992, *ApJ*, 396, L69
- Scaife, A. M. M., Nikolic, B., Green, D. A., et al. 2010, *MNRAS*, 406, L45
- Schlegel, D. J., Finkbeiner, D. P., & Davis, M. 1998, *ApJ*, 500, 525
- Tabatabaei, F. S., Beck, R., Krügel, E., et al. 2007, *A&A*, 475, 133
- Tammann, G. A. 1982, in *NATO ASIC Proc. 90: Supernovae: A Survey of Current Research*, ed. M. J. Rees & R. J. Stoneham, 371–403
- Turner, J. L., Beck, S. C., Crosthwaite, L. P., et al. 2003, *Nature*, 423, 621
- Turner, J. L., & Ho, P. T. P. 1983, *ApJ*, 268, L79
- . 1985, *ApJ*, 299, L77
- . 1994, *ApJ*, 421, 122
- Turner, J. L., Ho, P. T. P., & Beck, S. C. 1998, *AJ*, 116, 1212
- Walterbos, R. A. M., & Greenawalt, B. 1996, *ApJ*, 460, 696
- Weingartner, J. C., & Draine, B. T. 2001, *ApJ*, 548, 296
- Wu, H., Cao, C., Hao, C., et al. 2005, *ApJ*, 632, L79
- Zhu, Y., Wu, H., Cao, C., & Li, H. 2008, *ApJ*, 686, 155

## APPENDIX

Here we present the more detailed results from the GBT observations, as well as summarize all star formation rate equations either utilized or empirically derived in the present analysis. For the GBT observations, we give the flux densities and errors reported from the four individual CCB ports, and provide details on how much time was spent on each source in Tables 6 and 7. We again note that the flux densities of the individual channels reported here do not include any corrections. Upper limits for the individual channels are not given, but rather actual measured values and estimated errors are given.

In Table 8 we provide a summary of the theoretical and empirically derived star formation rate calibrations from this paper. A thorough discussion of the theoretical derivations can be found in §3.3 and in Murphy et al. (2011), while details on the empirically derived, dust-dependent star formation rate estimates are given in §4.2 and 4.3. We also provide the timescale for the emission of each star formation rate diagnostic to fade to 50 and 5% of its peak value after having had 100 Myr of continuous star formation come to a halt. These timescales, which are sensitive to the exact star formation history, were estimated using Starburst99 (Leitherer et al. 1999) following the same assumptions that went into deriving the corresponding theoretical relations as described in §3.3 and in the table caption. Additional considerations for the radiating times of CR electrons were included when calculating the fading time for the non-thermal radio continuum emission, the details of which can be found in Murphy (2009).

**Table 6**  
Nuclear Photometry for Individual CCB Ports

Galaxy	$S_{22.75 \text{ GHz}}$ (mJy)	$S_{31.25 \text{ GHz}}$ (mJy)	$S_{34.75 \text{ GHz}}$ (mJy)	$S_{38.25 \text{ GHz}}$ (mJy)	$\nu_{\text{eff}}$ (GHz)	$N_{\text{nods}}$ used/taken	$t_{\text{on}}$ (min)
NGC 337	$3.5 \pm 0.39$	$2.7 \pm 0.26$	$2.5 \pm 0.34$	$2.1 \pm 0.34$	33.11	8/ 8	5.3
NGC 628	$0.1 \pm 0.09$	$-0.0 \pm 0.06$	$-0.1 \pm 0.05$	$-0.0 \pm 0.08$	33.18	43/60	28.7
NGC 855	$0.9 \pm 0.08$	$0.7 \pm 0.05$	$0.6 \pm 0.05$	$0.6 \pm 0.08$	33.11	48/60	32.0
NGC 925	$0.7 \pm 0.06$	$0.6 \pm 0.04$	$0.4 \pm 0.05$	$0.4 \pm 0.08$	32.83	60/77	40.0
NGC 1266	$9.8 \pm 0.35$	$9.6 \pm 0.25$	$8.2 \pm 0.34$	$7.6 \pm 0.33$	33.24	8/ 8	5.3
NGC 1377	$-0.2 \pm 0.35$	$-0.2 \pm 0.25$	$-0.2 \pm 0.33$	$-0.5 \pm 0.32$	32.48	8/ 8	5.3
IC 342	$29.7 \pm 0.27$	$27.6 \pm 0.17$	$25.0 \pm 0.18$	$23.3 \pm 0.16$	33.29	8/ 8	5.3
NGC 1482	$12.8 \pm 0.34$	$13.1 \pm 0.24$	$10.6 \pm 0.33$	$9.1 \pm 0.32$	33.58	8/ 8	5.3
NGC 2146	$99.8 \pm 0.21$	$85.5 \pm 0.19$	$73.7 \pm 0.14$	$64.9 \pm 0.24$	33.80	4/ 4	2.7
NGC 2403	$0.3 \pm 0.08$	$0.1 \pm 0.06$	$0.1 \pm 0.05$	$0.1 \pm 0.09$	32.88	23/23	15.3
Holmberg II	$0.9 \pm 0.04$	$0.7 \pm 0.03$	$0.7 \pm 0.03$	$0.6 \pm 0.04$	33.36	70/70	46.7
NGC 2798	$10.0 \pm 1.10$	$8.9 \pm 0.94$	$7.8 \pm 0.35$	$6.6 \pm 0.60$	34.15	1/ 2	0.7
NGC 2841	$1.7 \pm 0.06$	$1.6 \pm 0.06$	$1.6 \pm 0.04$	$1.5 \pm 0.06$	32.84	50/50	33.3
NGC 2976	$0.3 \pm 0.25$	$0.1 \pm 0.16$	$0.4 \pm 0.09$	$0.2 \pm 0.20$	33.64	10/10	6.7
NGC 3049	$2.2 \pm 0.30$	$1.8 \pm 0.21$	$1.5 \pm 0.15$	$1.2 \pm 0.21$	33.78	4/ 4	2.7
NGC 3077	$9.1 \pm 0.32$	$8.4 \pm 0.24$	$7.4 \pm 0.14$	$6.6 \pm 0.26$	33.46	4/ 4	2.7
NGC 3190	$1.3 \pm 0.17$	$1.0 \pm 0.13$	$0.9 \pm 0.09$	$0.8 \pm 0.13$	33.59	10/10	6.7
NGC 3184	$0.2 \pm 0.18$	$0.2 \pm 0.13$	$0.1 \pm 0.09$	$0.2 \pm 0.13$	33.63	10/10	6.7
NGC 3198	$0.8 \pm 0.30$	$0.8 \pm 0.27$	$0.7 \pm 0.13$	$0.7 \pm 0.28$	33.57	4/ 4	2.7
IC 2574	$0.7 \pm 0.12$	$0.7 \pm 0.07$	$0.6 \pm 0.09$	$0.6 \pm 0.07$	33.46	54/54	36.0
NGC 3265	$1.2 \pm 0.37$	$1.3 \pm 0.30$	$1.2 \pm 0.20$	$0.7 \pm 0.24$	33.94	2/ 2	1.3
NGC 3351	$6.3 \pm 0.36$	$5.4 \pm 0.29$	$4.9 \pm 0.19$	$4.1 \pm 0.22$	33.85	2/ 2	1.3
NGC 3521	$2.2 \pm 0.18$	$1.8 \pm 0.17$	$1.2 \pm 0.10$	$1.3 \pm 0.18$	33.63	4/ 4	2.7
NGC 3627	$3.2 \pm 0.19$	$2.7 \pm 0.18$	$2.8 \pm 0.11$	$2.4 \pm 0.20$	33.05	4/ 4	2.7
NGC 3773	$1.1 \pm 0.09$	$1.0 \pm 0.10$	$0.9 \pm 0.12$	$0.8 \pm 0.20$	31.71	8/ 8	5.3
NGC 3938	$0.2 \pm 0.11$	$0.2 \pm 0.11$	$0.1 \pm 0.17$	$0.0 \pm 0.17$	31.17	42/44	28.0
NGC 4254	$2.1 \pm 0.27$	$1.8 \pm 0.22$	$1.6 \pm 0.11$	$1.2 \pm 0.21$	33.79	4/ 4	2.7
NGC 4321	$5.2 \pm 0.26$	$4.5 \pm 0.21$	$4.3 \pm 0.13$	$4.0 \pm 0.20$	33.33	4/ 4	2.7
NGC 4536	$20.2 \pm 0.26$	$18.5 \pm 0.21$	$17.2 \pm 0.11$	$16.5 \pm 0.20$	33.15	4/ 4	2.7
NGC 4559	$0.9 \pm 0.10$	$0.7 \pm 0.08$	$0.7 \pm 0.06$	$0.6 \pm 0.09$	33.31	21/30	14.0
NGC 4569	$2.3 \pm 0.25$	$2.0 \pm 0.21$	$1.8 \pm 0.12$	$1.5 \pm 0.20$	33.58	4/ 4	2.7
NGC 4579	$26.1 \pm 0.24$	$24.7 \pm 0.20$	$23.3 \pm 0.12$	$22.6 \pm 0.22$	32.98	4/ 4	2.7
NGC 4594	$75.3 \pm 0.08$	$74.5 \pm 0.06$	$71.8 \pm 0.07$	$65.4 \pm 0.14$	32.95	14/14	9.3
NGC 4625	$0.5 \pm 0.04$	$0.4 \pm 0.03$	$0.3 \pm 0.03$	$0.3 \pm 0.04$	33.21	50/50	33.3
NGC 4631	$6.4 \pm 0.14$	$4.7 \pm 0.15$	$3.4 \pm 0.11$	$3.0 \pm 0.20$	34.27	4/ 4	2.7
NGC 4725	$0.3 \pm 0.05$	$0.3 \pm 0.04$	$0.3 \pm 0.06$	$0.2 \pm 0.07$	32.01	42/74	28.0
NGC 4736	$3.7 \pm 0.15$	$3.2 \pm 0.15$	$2.6 \pm 0.11$	$2.5 \pm 0.21$	33.26	4/ 4	2.7
NGC 4826	$7.7 \pm 0.18$	$6.4 \pm 0.16$	$5.7 \pm 0.12$	$5.1 \pm 0.20$	33.61	4/ 4	2.7
NGC 5055	$3.2 \pm 0.47$	$2.9 \pm 0.37$	$2.4 \pm 0.33$	$2.0 \pm 0.76$	32.37	4/ 4	2.7
NGC 5194	$7.7 \pm 0.45$	$7.6 \pm 0.39$	$5.6 \pm 0.31$	$5.4 \pm 0.72$	32.91	4/ 4	2.7
NGC 5457	$-0.0 \pm 0.44$	$-2.2 \pm 0.39$	$-1.6 \pm 0.46$	$-0.9 \pm 1.11$	31.05	4/ 4	2.7
NGC 5474	$0.3 \pm 0.12$	$0.1 \pm 0.08$	$0.1 \pm 0.08$	$0.2 \pm 0.11$	32.99	53/57	35.3
NGC 5713	$8.5 \pm 0.43$	$7.2 \pm 0.37$	$6.1 \pm 0.14$	$5.3 \pm 0.28$	33.93	4/ 4	2.7
NGC 5866	$6.7 \pm 0.23$	$6.3 \pm 0.17$	$6.4 \pm 0.08$	$6.3 \pm 0.16$	32.77	12/12	8.0
NGC 6946	$19.9 \pm 0.16$	$17.4 \pm 0.23$	$15.3 \pm 0.18$	$13.9 \pm 0.25$	33.55	4/ 4	2.7
NGC 7331	$2.2 \pm 0.22$	$1.6 \pm 0.30$	$1.3 \pm 0.19$	$1.3 \pm 0.22$	34.48	3/ 4	2.0

**Table 7**  
Extranuclear Photometry for Individual CCB ports

ID	$S_{22.75 \text{ GHz}}$ (mJy)	$S_{31.25 \text{ GHz}}$ (mJy)	$S_{34.75 \text{ GHz}}$ (mJy)	$S_{38.25 \text{ GHz}}$ (mJy)	$\nu_{\text{eff}}$ (GHz)	$N_{\text{nods}}$ used/taken	$t_{\text{on}}$ (min)
NGC 628 Enuc. 1	0.6 ± 0.39	0.6 ± 0.29	0.6 ± 0.37	0.3 ± 0.38	32.48	7/ 7	4.7
NGC 628 Enuc. 2	0.4 ± 0.11	0.3 ± 0.08	0.4 ± 0.05	0.3 ± 0.09	33.51	40/40	26.7
NGC 628 Enuc. 3	0.6 ± 0.12	0.5 ± 0.08	0.5 ± 0.05	0.4 ± 0.09	33.49	37/40	24.7
NGC 628 Enuc. 4	0.1 ± 0.15	0.1 ± 0.08	0.1 ± 0.10	0.2 ± 0.12	32.95	37/60	24.7
NGC 2403 Enuc. 1	1.9 ± 0.36	1.9 ± 0.27	1.6 ± 0.14	1.5 ± 0.30	33.50	4/ 4	2.7
NGC 2403 Enuc. 2	1.7 ± 0.33	1.2 ± 0.24	1.5 ± 0.14	1.1 ± 0.29	33.31	4/ 4	2.7
NGC 2403 Enuc. 3	4.2 ± 0.33	3.6 ± 0.23	3.0 ± 0.13	2.3 ± 0.28	33.73	4/ 4	2.7
NGC 2403 Enuc. 4	1.7 ± 0.12	1.5 ± 0.08	1.3 ± 0.05	1.2 ± 0.11	33.37	24/24	16.0
NGC 2403 Enuc. 5	1.6 ± 0.82	1.7 ± 0.70	1.3 ± 0.24	0.9 ± 0.42	34.62	2/ 2	1.3
NGC 2403 Enuc. 6	0.9 ± 0.15	0.7 ± 0.08	0.8 ± 0.09	0.7 ± 0.11	33.08	59/59	39.3
NGC 2976 Enuc. 1	4.6 ± 0.31	4.0 ± 0.24	3.4 ± 0.13	3.2 ± 0.26	33.46	4/ 4	2.7
NGC 2976 Enuc. 2	2.0 ± 0.31	2.0 ± 0.25	2.1 ± 0.14	1.7 ± 0.27	33.21	4/ 4	2.7
NGC 3521 Enuc. 1	0.3 ± 0.05	0.2 ± 0.04	0.3 ± 0.04	0.2 ± 0.05	32.39	65/66	43.3
NGC 3521 Enuc. 2	1.2 ± 0.18	1.3 ± 0.21	0.9 ± 0.10	0.5 ± 0.18	33.37	4/ 4	2.7
NGC 3521 Enuc. 3	0.5 ± 0.05	0.4 ± 0.05	0.3 ± 0.05	0.3 ± 0.06	32.77	59/60	39.3
NGC 3627 Enuc. 1	3.0 ± 0.19	2.5 ± 0.18	2.3 ± 0.11	2.2 ± 0.20	33.17	4/ 4	2.7
NGC 3627 Enuc. 2	7.4 ± 0.18	6.7 ± 0.18	5.9 ± 0.11	5.6 ± 0.19	33.31	4/ 4	2.7
NGC 3627 Enuc. 3	0.9 ± 0.18	0.8 ± 0.19	0.5 ± 0.11	0.5 ± 0.20	33.17	4/ 4	2.7
NGC 3938 Enuc. 1	0.2 ± 0.05	0.1 ± 0.04	0.1 ± 0.03	0.1 ± 0.05	33.01	49/50	32.7
NGC 3938 Enuc. 2	0.4 ± 0.38	0.4 ± 0.44	0.3 ± 0.53	0.3 ± 0.62	31.23	44/44	29.3
NGC 4254 Enuc. 1	1.4 ± 0.10	1.2 ± 0.10	1.0 ± 0.13	0.8 ± 0.22	31.92	8/ 8	5.3
NGC 4254 Enuc. 2	0.0 ± 0.12	-0.0 ± 0.07	-0.1 ± 0.08	0.0 ± 0.10	32.94	50/50	33.3
NGC 4321 Enuc. 1	0.1 ± 0.10	0.1 ± 0.09	0.1 ± 0.08	-0.0 ± 0.11	32.52	43/51	28.7
NGC 4321 Enuc. 2	-0.4 ± 0.11	-0.3 ± 0.07	-0.2 ± 0.07	-0.2 ± 0.09	33.39	49/49	32.7
NGC 4631 Enuc. 1	1.1 ± 0.16	1.0 ± 0.10	1.0 ± 0.15	0.7 ± 0.17	32.43	25/50	16.7
NGC 4631 Enuc. 2	0.9 ± 0.12	0.8 ± 0.09	0.7 ± 0.07	0.5 ± 0.09	33.62	24/26	16.0
NGC 4736 Enuc. 1	3.3 ± 0.15	2.8 ± 0.15	2.6 ± 0.12	2.1 ± 0.21	33.15	4/ 4	2.7
NGC 5055 Enuc. 1	0.4 ± 0.21	0.1 ± 0.38	0.1 ± 0.26	0.2 ± 0.24	32.28	17/17	11.3
NGC 5194 Enuc. 1	0.8 ± 0.53	-4.3 ± 0.52	-3.3 ± 0.38	-0.3 ± 0.84	31.89	3/ 4	2.0
NGC 5194 Enuc. 2	2.9 ± 0.49	3.5 ± 0.43	0.9 ± 0.34	-0.1 ± 0.82	32.71	3/ 3	2.0
NGC 5194 Enuc. 3	1.2 ± 0.46	1.1 ± 0.47	1.1 ± 0.35	0.5 ± 0.75	32.15	4/ 4	2.7
NGC 5194 Enuc. 4	1.7 ± 0.45	2.7 ± 0.45	1.3 ± 0.34	2.5 ± 0.73	32.22	4/ 4	2.7
NGC 5194 Enuc. 5	1.9 ± 0.46	2.3 ± 0.51	1.9 ± 0.32	1.2 ± 0.69	32.39	4/ 4	2.7
NGC 5194 Enuc. 6	1.0 ± 0.14	0.9 ± 0.12	0.8 ± 0.07	0.9 ± 0.12	33.30	23/23	15.3
NGC 5194 Enuc. 7	0.8 ± 0.45	0.2 ± 0.51	0.6 ± 0.32	0.7 ± 0.69	32.41	4/ 4	2.7
NGC 5194 Enuc. 8	1.1 ± 0.51	-1.5 ± 0.60	2.1 ± 0.40	1.8 ± 0.81	32.05	3/ 4	2.0
NGC 5194 Enuc. 9	1.2 ± 0.44	0.8 ± 0.48	0.6 ± 0.35	0.5 ± 0.73	32.19	4/ 4	2.7
NGC 5194 Enuc. 10	0.8 ± 0.45	1.2 ± 0.47	0.3 ± 0.34	-0.8 ± 0.72	32.23	4/ 4	2.7
NGC 5194 Enuc. 11	-0.6 ± 0.20	-0.5 ± 0.23	-0.3 ± 0.16	-0.3 ± 0.24	32.65	14/14	9.3
NGC 5457 Enuc. 1	0.3 ± 0.17	0.7 ± 0.39	0.6 ± 0.28	0.5 ± 0.25	31.26	17/17	11.3
NGC 5457 Enuc. 2	0.3 ± 0.15	0.4 ± 0.15	0.2 ± 0.18	0.2 ± 0.19	31.93	32/40	21.3
NGC 5457 Enuc. 3	8.5 ± 0.54	9.1 ± 0.45	9.2 ± 0.55	7.4 ± 1.14	31.84	4/ 4	2.7
NGC 5457 Enuc. 4	2.4 ± 0.33	3.3 ± 0.26	1.3 ± 0.37	1.1 ± 0.86	31.48	7/ 7	4.7
NGC 5457 Enuc. 5	2.3 ± 0.47	2.8 ± 0.36	2.8 ± 0.49	2.8 ± 1.12	31.20	4/ 4	2.7
NGC 5457 Enuc. 6	3.1 ± 0.52	4.1 ± 0.38	3.7 ± 0.64	2.4 ± 1.37	31.02	3/ 3	2.0
NGC 5457 Enuc. 7	5.0 ± 0.45	5.1 ± 0.35	4.8 ± 0.54	4.5 ± 1.21	31.33	4/ 4	2.7
NGC 5713 Enuc. 1	1.8 ± 0.42	1.8 ± 0.42	1.0 ± 0.16	1.1 ± 0.28	34.28	4/ 4	2.7
NGC 5713 Enuc. 2	2.4 ± 0.42	1.7 ± 0.38	1.3 ± 0.16	1.3 ± 0.29	34.08	4/ 4	2.7
NGC 6946 Enuc. 1	0.3 ± 0.09	0.5 ± 0.08	0.5 ± 0.10	0.5 ± 0.12	31.70	16/16	10.7
NGC 6946 Enuc. 2	2.8 ± 0.17	2.6 ± 0.22	2.2 ± 0.21	2.1 ± 0.25	32.64	4/ 4	2.7
NGC 6946 Enuc. 3	1.2 ± 0.10	1.1 ± 0.09	0.9 ± 0.12	0.9 ± 0.13	32.52	15/16	10.0
NGC 6946 Enuc. 4	3.4 ± 0.10	3.2 ± 0.10	2.8 ± 0.12	2.7 ± 0.13	33.07	15/16	10.0
NGC 6946 Enuc. 5	0.6 ± 0.07	0.6 ± 0.07	0.4 ± 0.09	0.5 ± 0.08	32.37	37/37	24.7
NGC 6946 Enuc. 6	3.6 ± 0.16	3.1 ± 0.22	3.0 ± 0.21	2.2 ± 0.26	32.98	4/ 4	2.7
NGC 6946 Enuc. 7	3.6 ± 0.21	3.5 ± 0.24	3.0 ± 0.31	3.1 ± 0.29	32.48	3/ 4	2.0
NGC 6946 Enuc. 8	2.1 ± 0.19	1.9 ± 0.20	1.7 ± 0.26	1.7 ± 0.24	32.41	4/ 4	2.7
NGC 6946 Enuc. 9	3.1 ± 0.20	2.6 ± 0.20	2.4 ± 0.28	2.2 ± 0.23	32.81	4/ 4	2.7

**Table 8**  
Summary of Star Formation Rate Conversions

Observable	Equation	Fading Timescale <sup>a</sup>
Theoretical Relations <sup>b</sup>		
Extinction corrected FUV flux	$\text{SFR} = 4.42 \times 10^{-44} L_{\text{FUV}}$	$\sim 5, 100 \text{ Myr}$
Extinction corrected NUV flux	$\text{SFR} = 7.15 \times 10^{-44} L_{\text{NUV}}$	$\sim 5, 150 \text{ Myr}$
Extinction corrected H $\alpha$ recombination line flux	$\text{SFR} = 5.37 \times 10^{-42} L_{\text{H}\alpha}$	$\sim 2, 5 \text{ Myr}$
Free-free (radio) flux density	$\text{SFR} = 4.6 \times 10^{-28} T_{\text{e},4}^{-0.45} \nu_{\text{GHz}}^{0.1} L_{\nu}^{\text{T}}$	$\sim 2, 5 \text{ Myr}$
Non-thermal (radio) flux density	$\text{SFR} = 6.6 \times 10^{-29} \nu_{\text{GHz}}^{\alpha_{\text{NT}}} L_{\nu}^{\text{NT}}$	$\sim 40, 100 \text{ Myr}$
Total (radio) flux density	$\text{SFR} = 10^{-27} / (2.18 T_{\text{e},4}^{0.45} \nu_{\text{GHz}}^{-0.1} + 15.1 \nu_{\text{GHz}}^{-\alpha_{\text{NT}}}) L_{\nu}$	$\sim 2 - 40, 5 - 100 \text{ Myr}$
Empirical Relations <sup>c</sup>		
24 $\mu\text{m}$ flux density	$\text{SFR} = 2.45 \times 10^{-43} \nu L_{\nu}(24 \mu\text{m})$	$\sim 5, 100 \text{ Myr}$
Total infrared (IR; 8 – 1000 $\mu\text{m}$ ) flux	$\text{SFR} = 3.15 \times 10^{-44} L_{\text{IR}}$	$\sim 5, 100 \text{ Myr}$
24 $\mu\text{m}$ flux density and H $\alpha$ line flux	$\text{SFR} = 5.37 \times 10^{-42} [L_{\text{H}\alpha} + 0.018 \nu L_{\nu}(24 \mu\text{m})]$	$\sim 2 - 5, 5 - 100 \text{ Myr}$
Total IR and FUV fluxes	$\text{SFR} = 4.42 \times 10^{-44} (L_{\text{FUV}} + 0.50 L_{\text{IR}})$	$\sim 5, 100 \text{ Myr}$

<sup>a</sup> The timescales given are those for the emission to drop to 50 and 5% of its peak value after having had 100 Myr of continuous star formation come to a halt. These values, which are sensitive to the star formation history, were calculated using Starburst99 (Leitherer et al. 1999) following the same assumptions that went into deriving the corresponding theoretical relations. The non-thermal radio continuum timescale sums the fading timescale of supernovae activity and appropriate fractions of the radiating lifetimes for 1.4 GHz emitting CR electrons in the ISM assuming a magnetic field strength of 5  $\mu\text{G}$ , equipartition between the magnetic and radiation field energy densities, and an ISM density of  $n_{\text{ISM}} = 0.1 \text{ cm}^{-3}$  (for details on the CR cooling timescales see Murphy 2009).

<sup>b</sup> Each theoretical calibration was calculated using using Starburst99 (Leitherer et al. 1999) and assumes solar metallicity, continuous star formation, and a Kroupa (2001) IMF, having a slope of  $-1.3$  for stellar masses between  $0.1 - 0.5 M_{\odot}$  and  $-2.3$  for stellar masses ranging between  $0.5 - 100 M_{\odot}$ . Star formation rates are in units of  $M_{\odot} \text{ yr}^{-1}$  and observables are in cgs units. The UV calibrations are calculated using the *GALEX* FUV and NUV basspands, which are centered at 1528 and 2271  $\text{\AA}$ , respectively. For radio-based star formation rates,  $\nu_{\text{GHz}}$  and  $T_{\text{e},4}$  are frequency and thermal electron temperature in units of GHz and  $10^4 \text{ K}$ , respectively. Additionally,  $\alpha_{\text{NT}}$  is the non-thermal radio spectral index, which is assumed to be  $\sim 0.85$  in the present analysis.

<sup>c</sup> The empirical relations each have a scatter that is roughly a factor of  $\lesssim 2$ . Consequently, the empirical calibration given here for the total IR luminosity is consistent with the theoretical relation given in Murphy et al. (2011,  $\text{SFR} = 3.88 \times 10^{-44} L_{\text{IR}}$ ), which, using starburst99 with the same assumptions above, assumed that the entire Balmer continuum was absorbed and reradiated in the infrared. See §3.3, 4.2, and 4.3 for more details.

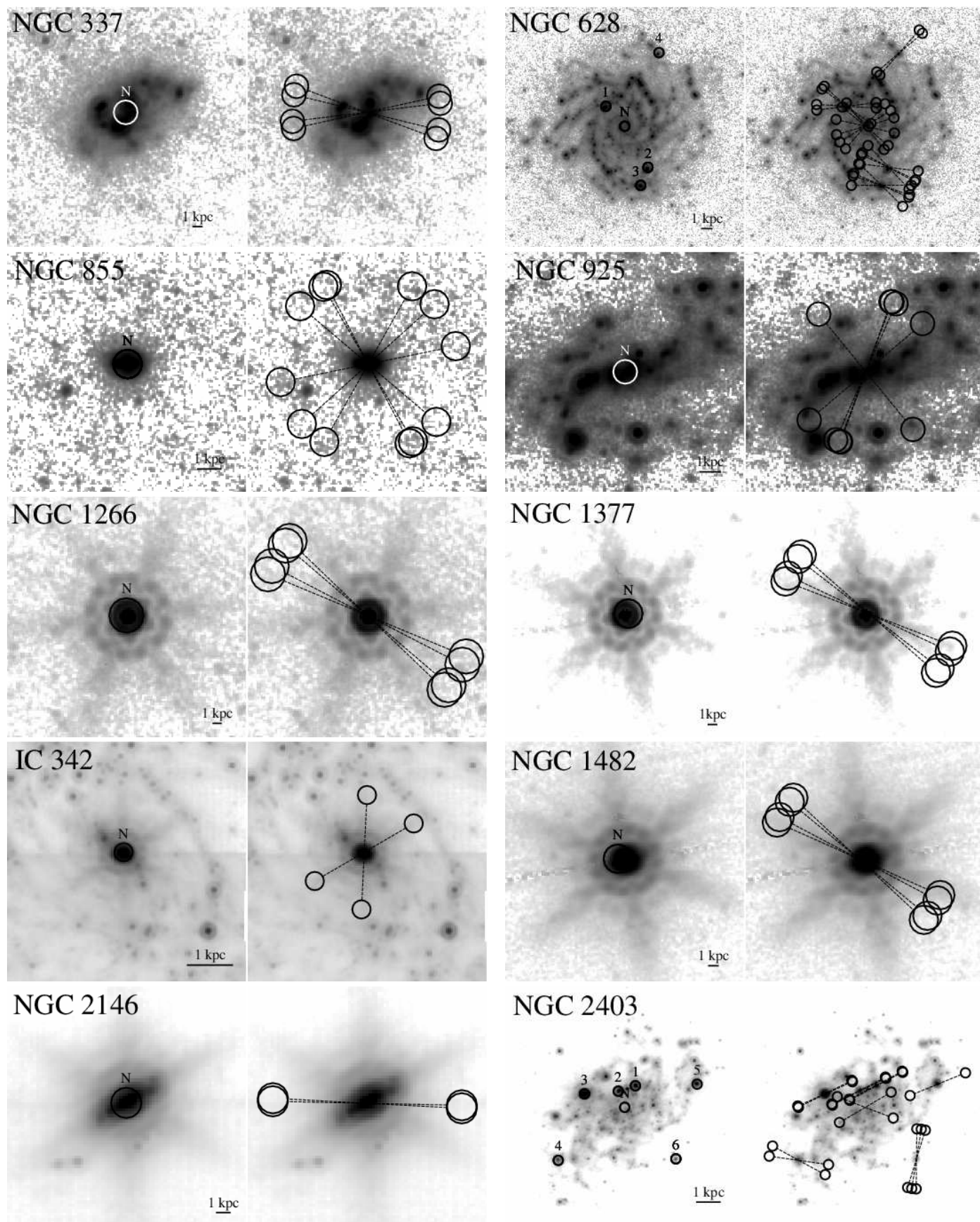


**Figure 1.** For each galaxy we show 2 side-by-side panels illustrating the GBT observations on  $24\ \mu\text{m}$  *Spitzer* images. The left panels indicate the location of each GBT 33 GHz pointing, while the right panels show the location of the GBT reference nod positions (see §2.2). The diameter of each circle is  $25''$ , which corresponds to the typical FWHM of the GBT beam at 33 GHz. The 1 kpc linear scale bars assume the distances given in Table 1.

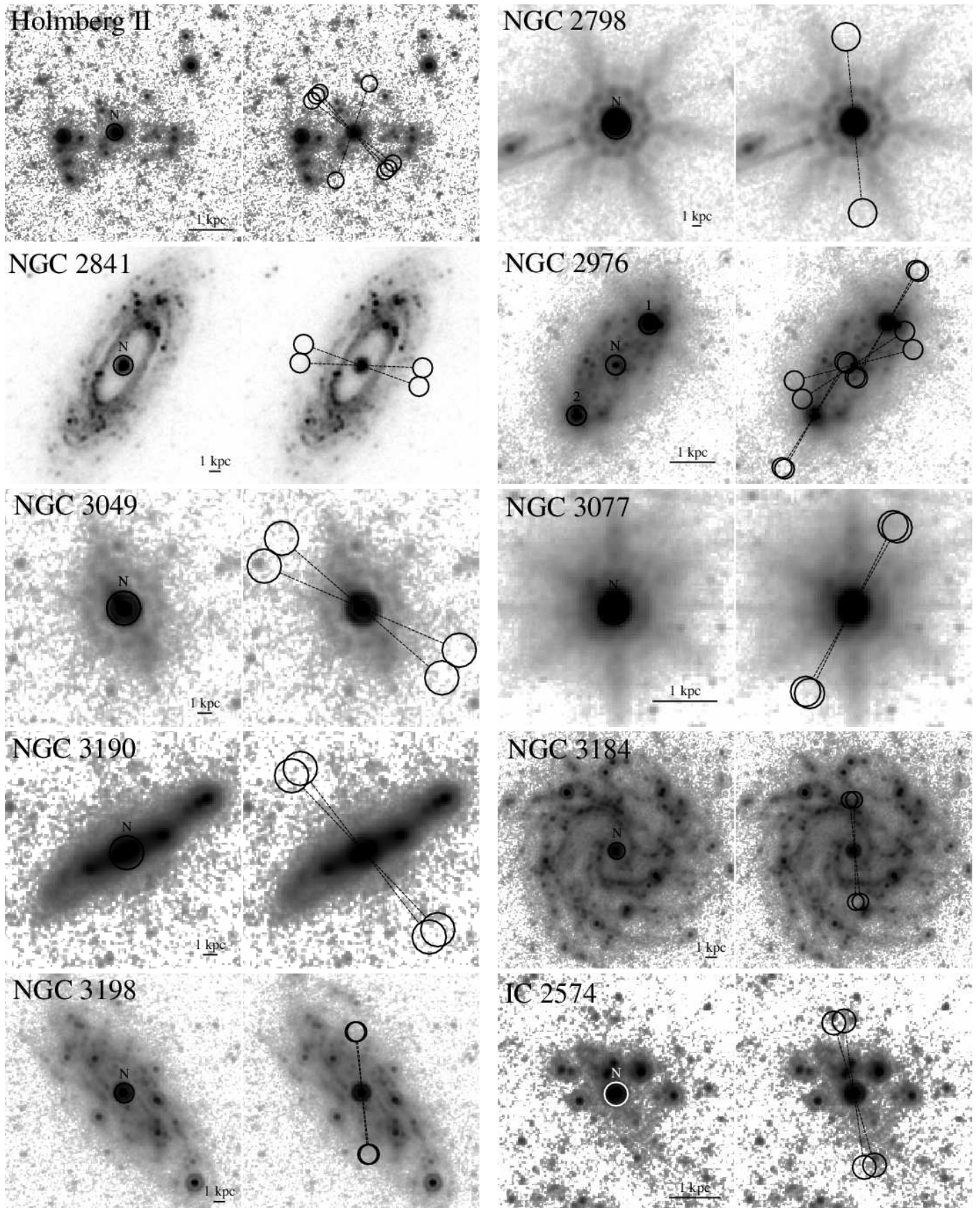


Figure 1. *Continued*

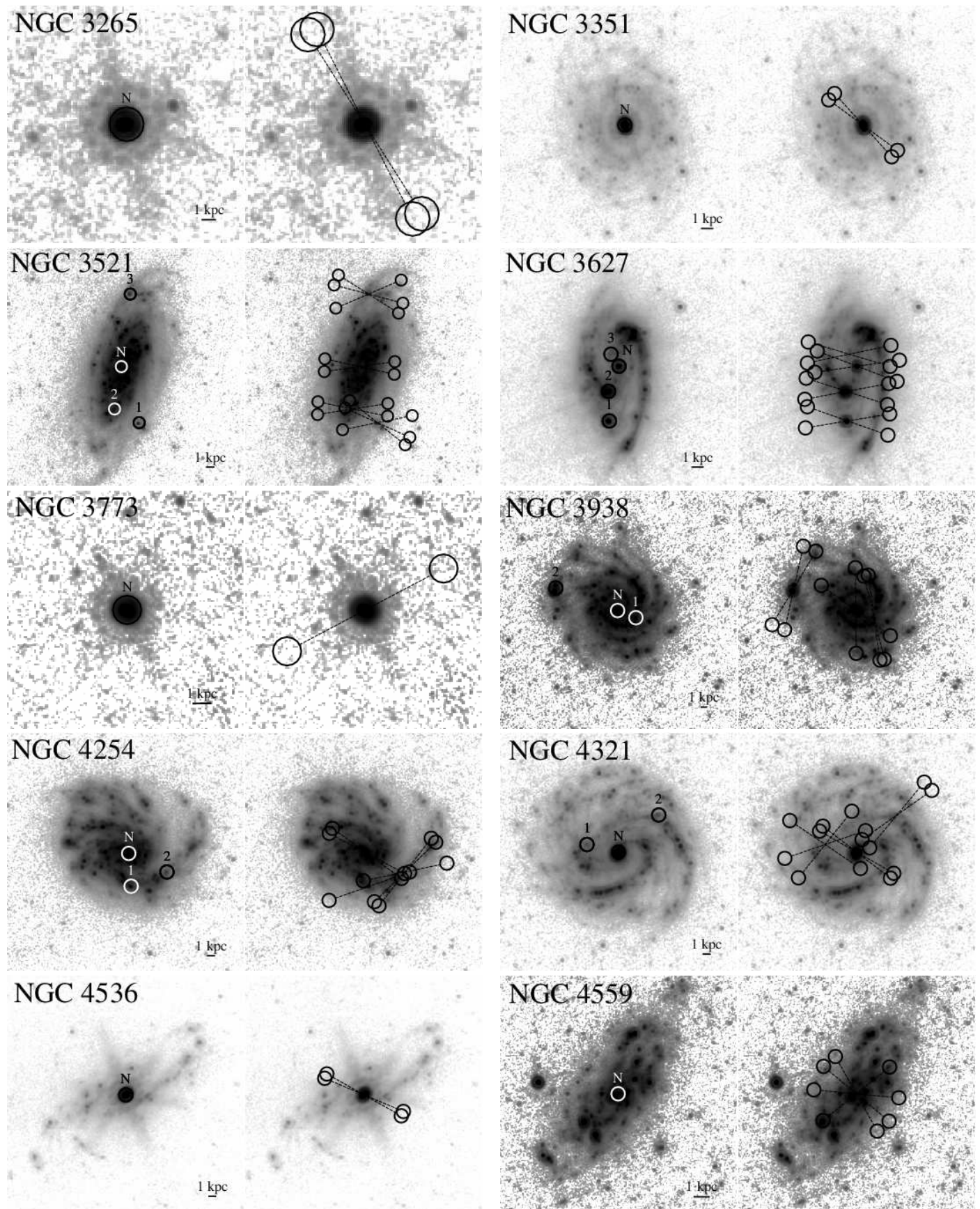


Figure 1. *Continued*

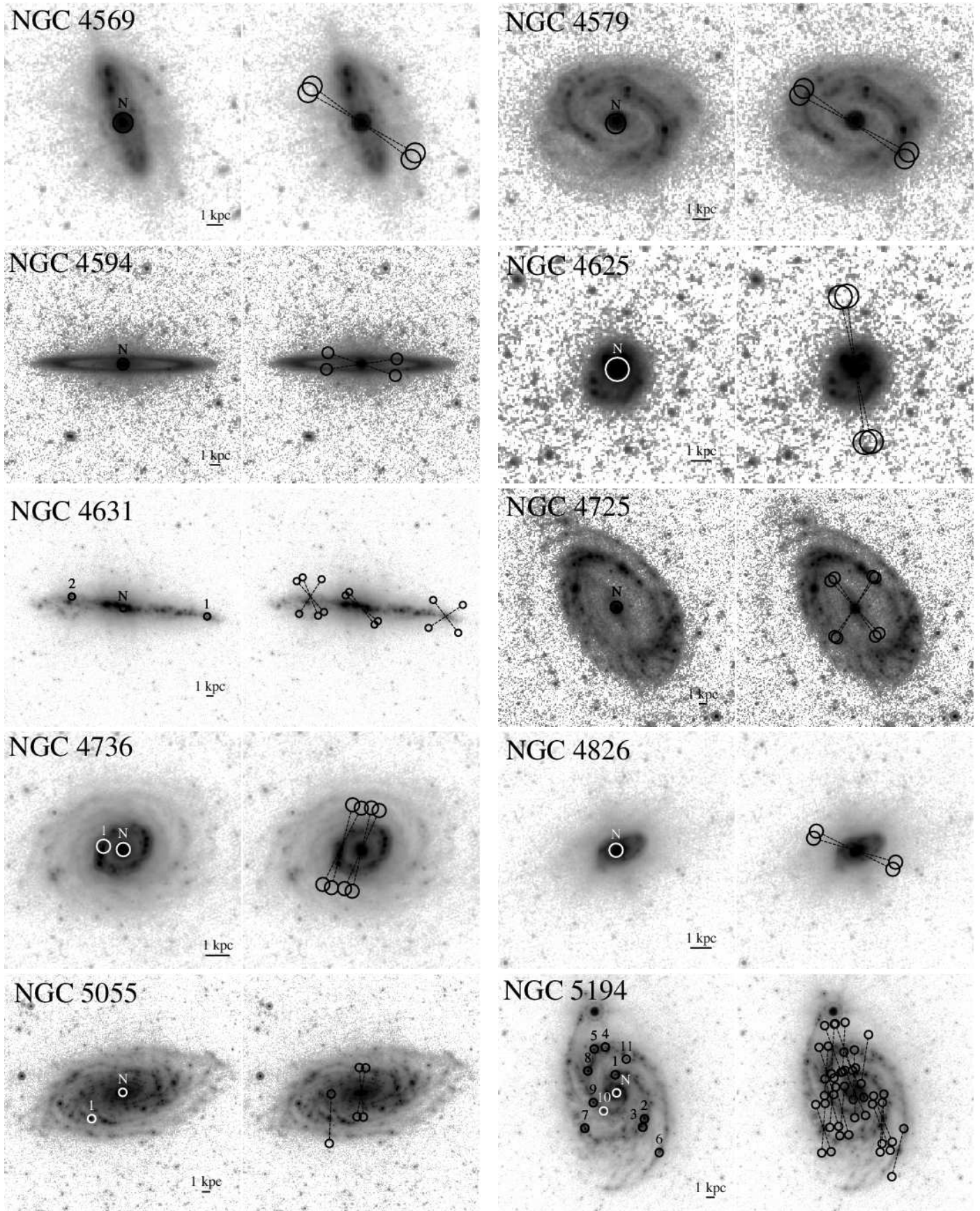


Figure 1. *Continued*

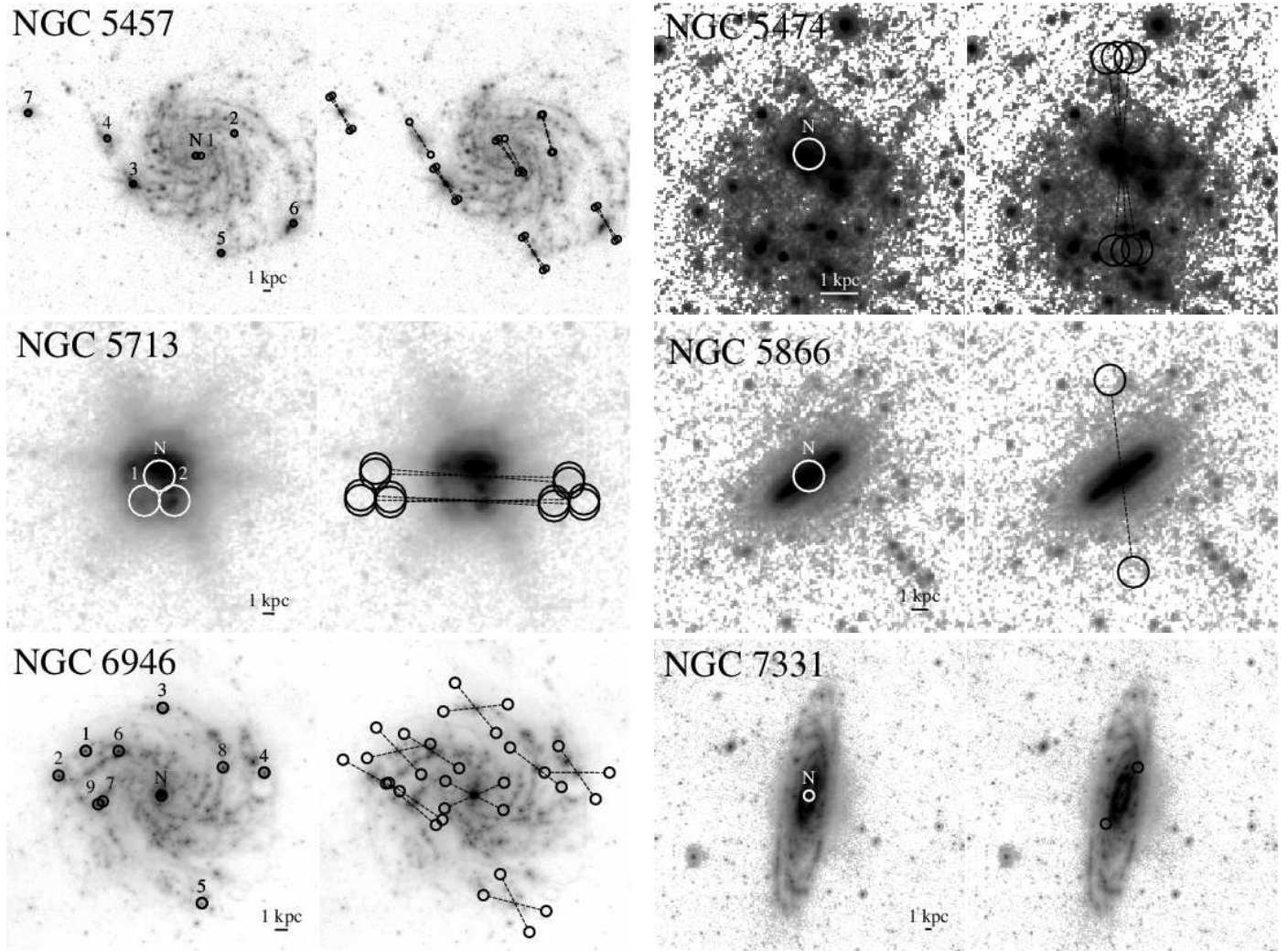


Figure 1. *Continued*